Ore Geology Reviews 105 (2019) 123–136

Contents lists available at ScienceDirect

Ore Geology Reviews

journal homepage: www.elsevier.com/locate/oregeorev

In situ trace element and sulfur isotope of pyrite constrain ore genesis in the Shapoling molybdenum deposit, East Qinling Orogen, China

Xin-Kai Hu[a], Li Tang[a,*], Shou-Ting Zhang[a,*], M. Santosh[a,b], Christopher J. Spencer[c], Yu Zhao[a], Hua-Wen Cao[d], Qiu-Ming Pei[e]

[a] School of Earth Sciences and Resources, China University of Geosciences Beijing, 29 Xueyuan Road, Beijing 100083, China
[b] Centre for Tectonics, Exploration and Research, University of Adelaide, Adelaide, SA 5005, Australia
[c] School of Earth and Planetary Sciences, The Institute of Geoscience Research, Curtin University, Perth, WA 6845, Australia
[d] Chengdu Center, China Geological Survey, Chengdu 610081, China
[e] Faculty of Geosciences and Environmental Engineering, Southwest Jiaotong University, Chengdu 611756, China

ARTICLE INFO

Keywords:
Pyrite
Trace element
Sulfur isotope
Shapoling Mo deposit
East Qinling

ABSTRACT

The Early Cretaceous (ca. 128 Ma) Shapoling vein-type molybdenum (Mo) mineralization, associated with the Huashan intrusion is a newly discovered deposit in the Xiong'ershan district, East Qinling, China where pyrite is a ubiquitous mineral phase. Here we present results from an integrated study on the texture, *in situ* trace element chemistry from laser ablation inductively coupled plasma mass spectrometry (LA-ICP-MS) and sulfur isotopic composition using secondary-ion mass spectrometry (SIMS), with a view to understand the geochemical variation, genesis of Mo mineralization and ore-forming process. The distinct textural patterns as revealed by petrographic observations suggest three types of pyrites: Py1 is composed of coarse-grained euhedral pyrite in the wall rock and early barren quartz vein at Stage I, Py2 is represented by subhedral-anhedral grains coexisting with molybdenite in quartz veins at Stage II, and Py3 forms irregular interstitial grains in the quartz + K-feldspar + molybdenite dominated veins at Stage III. The Mo enrichment mainly occurred in Py3 (with Co/Ni ratios > 1 and $\delta^{34}S$ values mainly < 0‰). Our study shows that Mo, Au, Pb, Zn, Ag and Cu are selectively partitioned into pyrite as mineral micro/nano-inclusions, and that the siderophile and chalcophile elements (such as Co, Ni, As, Se and Te) occur substituted within different textural types of pyrite. The $\delta^{34}S$ values of the pyrites in Py1 and Py2 range between −2.33‰ and −0.37‰, indicating a dominantly magmatic origin. The $\delta^{34}S$ values of Py3 increase from −2.55‰ to +1.48‰. *In situ* $\delta^{34}S$ analysis of pyrite from Py1, Py2 to Py3 shows a progressive and gradual change in redox conditions. The negative values indicate oxidized sulfur in the early generation of pyrite (Py1 that coexists with magnetite). Conversely, positive values represent reduced sulfur found in the later generations of pyrite (Py3), which contain higher concentrations of Cu, Pb, Zn and Ag. The Mo-bearing pyrite identified in our study could be used as a possible pathfinder for the exploration of high-grade Mo mineralization.

1. Introduction

The East Qinling Mo belt (EQMB) in central China (Fig. 1) is one of the world's most important Mo provinces, which hostsnumerous molybdenum deposits with molybdenum metal reserves of 8.43 million tonnes (Mao et al., 2011). This region has been a focus of mineral exploration and scientific research for many years in relation to the Mesozoic porphyry-related deposits including porphyry, porphyry-skarn and skarn types of deposits (Chen et al., 2000; Li et al., 2007; Mao et al., 2008, 2011; Zhang et al., 2011; Bao et al., 2017; Lu et al., 2017). Diverse types of Mo deposits have been reported in vein systems in the EQMB, such as in quartz-vein systems (e.g. Deng et al., 2016, 2017), carbonatite-vein systems (e.g. Huang et al., 2009; Cao et al., 2014), and fluorite-vein systems (e.g. Deng et al., 2014b, 2015). These vein systems show remarkable difference in their geological and geochemical features and isotope ages leading to controversies on their genesis. The molybdenum ores occur in diverse vein systems such as in quartz – dominated veins, carbonatite – dominated veins, and fluorite – dominated veins. The available geochemical data suggest that the ore forming elements and fluids in these veins came from different sources (Deng et al., 2013b,c, 2014c). The published molybdenite Re–Os ages display a large scatter in ages from Palaeoproterozoic (ca. 1.85 Ga,

* Corresponding authors.
E-mail addresses: ltang@cugb.edu.cn (L. Tang), zst@cugb.edu.cn (S.-T. Zhang).

https://doi.org/10.1016/j.oregeorev.2018.12.019
Received 11 March 2018; Received in revised form 28 October 2018; Accepted 19 December 2018
Available online 20 December 2018
0169-1368/

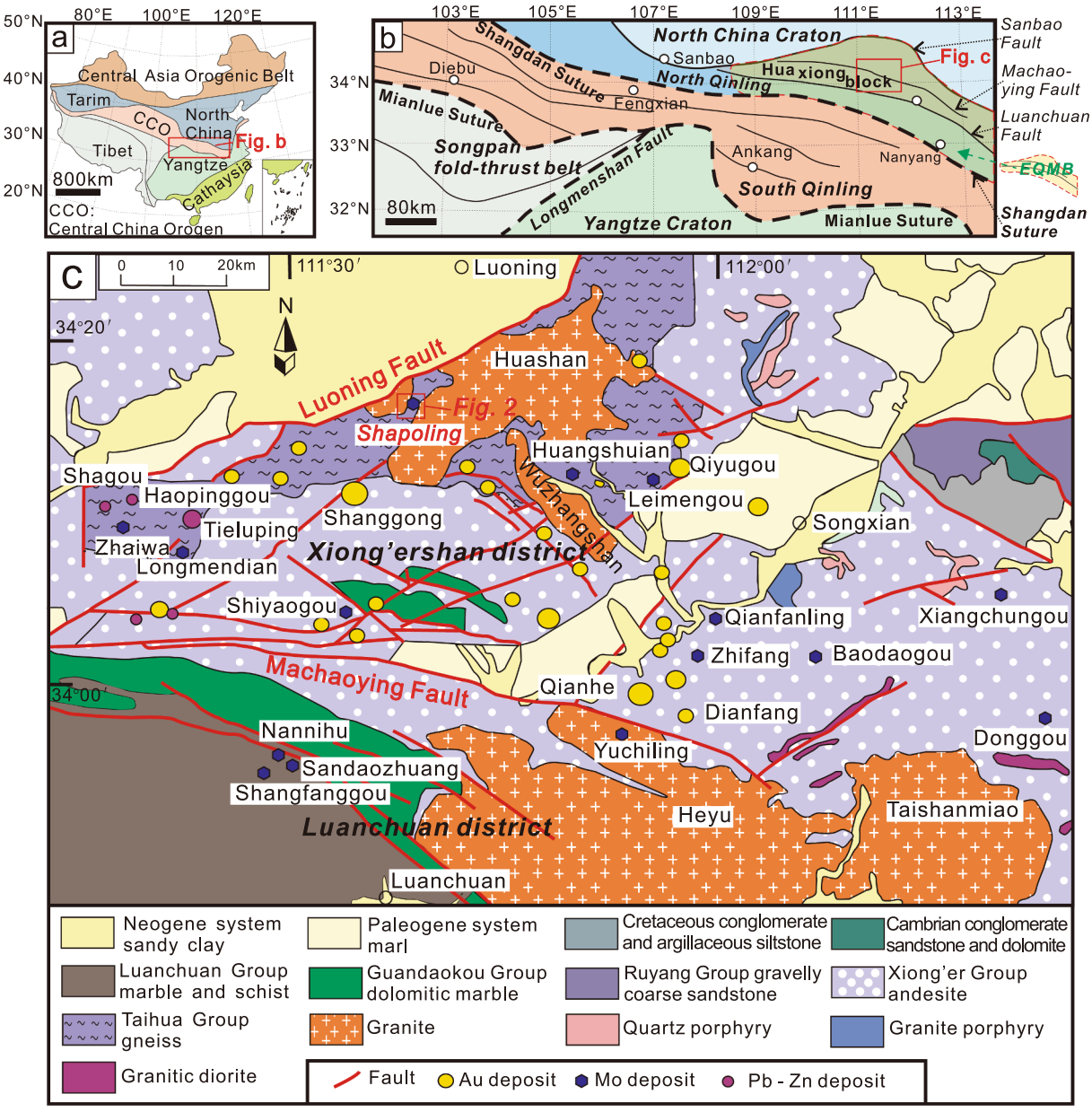

Fig. 1. Geological maps, showing the major tectonic subdivisions of China and the location of Qinling Orogen (a); tectonic framework of the Qinling Orogen (b); geology and distribution of the mineral deposits in the Xiong'ershan district (c) (modified after Deng et al. (2014a) and Cao et al. (2015)).

Deng et al., 2013a) to Early Cretaceous (Liu et al., 2011). Furthermore, the diverse styles of mineralization associated with these deposits include: (1) orogenic type Mo deposits related to the Indosinian Orogeny (Deng et al., 2014b; Li and Pirajno, 2017), (2) strata-bound deposits related to a Paleo- to Mesoproterozoic volcanic hydrothermal event (Bai and Xiao, 2009; Bai et al., 2009b, 2010), (3) vein type Mo deposits generated during post-collisional extension following the amalgamation of the North China and Yangtze Cratons (Huang et al., 2009; Cao et al., 2014; Li and Pirajno, 2017), and (4) strata-bound or vein type Mo deposits associated with Yanshanian magmatism (Wen et al., 2008; Zhao et al., 2015). The mechanisms of ore genesis, as well as the source(s) of ore-forming elements and fluid remain controversial. Characterizing the mineralization and genesis of the Mo-bearing vein systems is fundamental to the modelling of Mo deposits in EQMB and exploration targeting.

The Shapoling Mo deposit in the Xiong'ershan district of the EQMB is a typical vein system with the following salient features. (1) The orebodies are defined by the concentration of numerous thin Mo-bearing quartz veins controlled by fault zones; (2) the Mo mineralization occurred in Early Cretaceous as suggested by the molybdenite Re-Os isochron age of 128.1 ± 7.1 Ma (Su et al., 2009; Liu et al., 2011), broadly contemporaneous with the emplacement age of the spatially related Huashan pluton; and (3) the remarkably high Re content in molybdenite (147–307 ppm) suggests the involvement of mantle sourced fluid. Previous studies addressed the ore geology and timing of mineralization, although the mechanism of ore genesis remains unclear (Cui et al., 2006; Chen, 2009; Su et al., 2009; Liu et al., 2011).

Pyrite is the most abundant sulfide in the Earth's crust and is also a major constituent of hydrothermal mineralization in a wide variety of ore systems, including porphyry copper deposits, volcanogenic massive sulfide deposits, iron-oxide-copper-gold deposits, sedimentary rock hosted copper/uranium deposits, and Archean to Mesozoic lode, epithermal and Carlin-type gold deposits, among others (Reich et al., 2013). Pyrite also is the predominant sulfide mineral in the Shapoling Mo deposit. The trace element geochemistry of pyrite is an important proxy for monitoring the changes in pH, oxidation state and source of

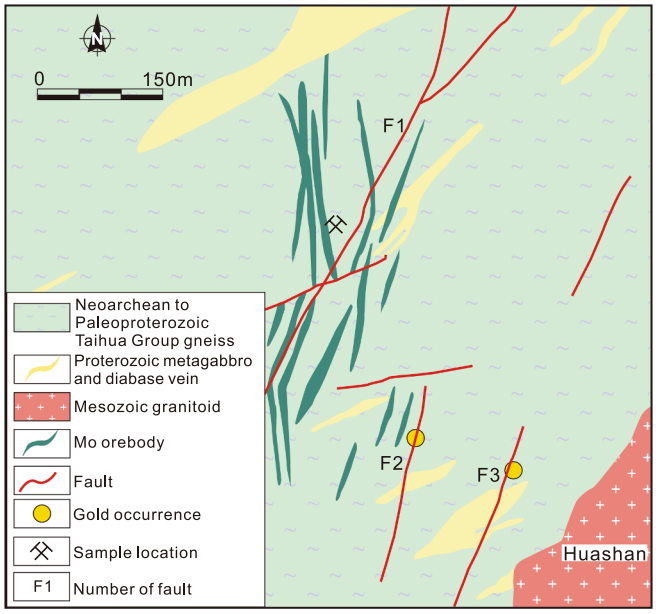

Fig. 2. Geological map of the Shapoling Mo deposit in the Xiong'ershan district (modified after Liu et al. (2011)).

the ore-forming fluid (e.g., Zhao et al., 2011; Zhang et al., 2014; Li et al., 2016; Ward et al., 2017). It has been noted that even in the case where trace element content of pyrite reflects nanoscale minerals or inclusions, the information provides a passive record of the chronological history of cyclical metal saturation in the parent fluid (Tanner et al., 2016). Sulfur isotopic composition of pyrite can be effectively used to evaluate the physicochemical conditions during deposition and provides an alternative technique to identify fluid source(s) or fluid mixing (e.g., Ulrich et al., 2011; Xue et al., 2013; Li et al., 2017a; Yan et al., 2018).

Although extensive studies were carried out on trace element and sulfur isotope in pyrite, coupled in situ trace element and sulfur isotope analyses on pyrite crystals from a Mo deposit has not been widely attempted. In this paper, we report an integrated in situ trace element and sulfur isotope analysis of pyrite from the Shapoling vein-type Mo deposit. We summarize the geologic setting and hydrothermal alteration of the Shapoling deposit, recognize three pyrite types and describe their textural characteristics from three stages of mineralization, and compare the changes in sulfur isotopes and trace element abundances. Our results provide insights into the hydrothermal process related to the mineralization and help in assessing the sources of ore-forming fluid and ore-forming material, with implications on ore genesis.

2. Regional geology

The Qinling Orogen is located at the central part of the E-W trending Central China Orogenic Belt (CCOB) that evolved from the northernmost Paleo-Tethys Ocean (Li et al., 2017b). The formation of this orogen involved Paleozoic to Mesozoic subduction-collision-accretion processes between the North China Craton and Yangtze Craton (Fig. 1a; Li et al., 2012, 2015; Dong and Santosh, 2016; Tang et al., 2016; Wang et al., 2017a). The Qinling Orogen has been subdivided into four tectonic units from north to south: the Huaxiong Block representing the reactivated southern margin of the NCC, North Qinling Belt, South Qinling Belt and northern South China Block with the San-bao, Luanchuan, Shangdan, Mianlue and Longmenshan faults as their boundaries (Fig. 1b; Chen et al., 2014b). The main lithostratigraphic units of the Huaxiong Block consist of crystalline basement of the Late Neoarchean-Paleoproterozoic Taihua Group, the lowest cover of the Mesoproterozoic Xiong'er Group, and the Meso- to Neoproterozoic Guandaokou and Luanchuan Groups (Fig. 1c; Cao et al., 2015; Wang et al., 2016a,b). The Taihua Group is traditionally divided into an upper unit composed of graphite-bearing gneiss, banded iron formation and amphibolite, and a lower unit represented by amphibolite- to granulite-facies metamorphosed tonalite-trondhjemite-granodiorite (TTG) gneiss and amphibolite (Tang et al., 2015; Zhang et al., 2015). The Xiong'er Group unconformably overlies the Taihua Group, and is mainly preserved as a weakly metamorphosed volcanic sequence composed of andesites, basaltic andesites, dacites and rhyolites. The Meso- to Neoproterozoic sedimentary sequences represented by the Guandaokou and Luanchuan Groups are mainly composed of carbonate rocks and clastic sedimentary rocks (Tang et al., 2018).

The Xiong'ershan district is bounded by the Luoning fault to the north and the Machaoying fault to the south, and is located at the central part of the Huaxiong Block (Fig. 1b). There are many ore deposits in the Xiong'ershan district, including porphyry Mo deposits (Leimengou and Shiyaogou), quartz-vein Mo deposits (Shapoling, Qianfanling and Zhifang) (Liu et al., 2011; Mao et al., 2011), carbonatite-vein Mo deposit (Huangshui'an) (Cao et al., 2014), breccia pipe hosted Au deposits (Qiyugou and Dianfang) (Chen et al., 2009; Fan et al., 2011; Tian et al., 2017), orogenic gold lodes (Shanggong) (Mao et al., 2002; Chen et al., 2008), and epithermal Ag-Pb-Zn deposits (Tieluping, Haopinggou and Shagou) (Chen et al., 2004; Li et al., 2013, 2016) (Fig. 1c). The Machaoying fault zone is the main geologic structure in the Xiong'ershan district, extending ~200 km WNW, and is a north-dipping thrust zone formed during Mesozoic continental collision (Fig. 1c). This fault zone controls many of the hydrothermal mineral systems in this area and was active until the late Cretaceous (Han et al., 2009).

3. Deposit geology

The Shapoling Mo deposit is located at the northwestern part of the Xiong'ershan district (Fig. 1c). The exposed strata in the Shapoling ore district comprise the Neoarchean to Paleoproterozoic Taihua Group, consisting of biotite and plagioclase gneisses, amphibole plagiogneiss, and amphibolite. The magmatic suites were emplaced during two phases, in Proterozoic and Mesozoic. The former includes gabbro-diabase stocks and sills, and the latter is represented by the Huashan batholith which is related to the Yanshanian tectonothermal event and comprises porphyritic biotite monzogranites, monzogranites and monzonite (Wang et al., 2016c). The orebodies are composed of numerous thin Mo-bearing quartz veins that occur within the contact zones between the Huashan pluton and Taihua Group (Fig. 2). The deposit is characterized by abundant stockworks of K-feldspar + quartz + pyrite + molybdenite veins. Most of the K-feldspar + quartz + pyrite + molybdenite veins extend along strike with a thickness ranging approximately 0.01 to 0.5 m. The orebodies are primarily vein type, and their morphology is controlled by the F1, F2, F3 fault zones (Fig. 2). The majority of these orebodies are controlled by NS- or NNE-trending fractures that dip to SE at angles of 40°–60°. A few of the orebodies strike NE and NW. The orebodies are 150 m–620 m long, with a thickness of 3–6 m. The deposit has total reserves of 8461 tones Mo at an average grade of 0.08%.

The major ore minerals of the Shapoling deposit include molybdenite, pyrite, and minor galena, chalcopyrite, sphalerite and scheelite. Molybdenite occurs as curved and coarse-grained flakes or flaky aggregates, filling fractures, or as spotted and sparsely disseminated ores in quartz + K-feldspar veins and K-feldspar altered rocks. Molybdenite also occurs as thin film within the altered rocks. The main gangue minerals are quartz and feldspar, with few sericite, garnet, carbonate, fluorite, chlorite and epidote. The alteration types include K-feldspathitization, silicification, sericitization, propylitic alteration, and carbonatization.

Hydrothermal alteration in the Shapoling deposit is extensive and is structurally controlled by the F1, F2 and F3 fault zones. Molybdenum

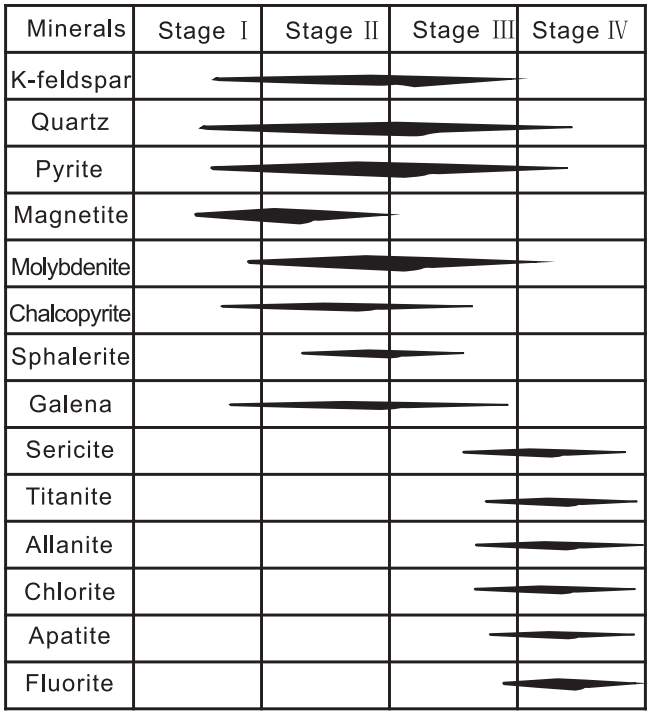

Fig. 3. Paragenetic sequence of the Shapoling Mo deposit. The widths of the lines denote relative abundance of minerals; the lines indicate local presence of a mineral.

mineralization is spatially associated with silicification, potassic and phyllic alteration, with a complex mineral assemblage. Based on mineral assemblage and crosscutting relationships, four stages of mineralization can be distinguished from early to late, as described below (Fig. 3).

Stage I: Stage I comprises mainly milky, massive and barren quartz, magnetite and minor coarse-grained euhedral pyrite which is labelled as Py1 (Figs. 4a, b and 5a, b). K-feldspathitization is also observed in the altered rocks, as exemplified by reddish massive and banded feldspathoid rocks. The barren quartz and pyrite veins extend along strike with cracks or dissemination in the altered rock, and are commonly crosscut by later sulfide-bearing veinlets, suggesting pre-ore feature (Fig. 4c, d).

Stage II: This stage is defined by quartz, pyrite and molybdenite, with minor galena, sphalerite, and chalcopyrite (Figs. 3 and 4c, d). Quartz is glassy to glassy-white in color and is more transparent than the earlier quartz, commonly displaying subhedral to euhedral nature. The pyrite in Stage II is subhedral-anhedral, and generally forms disseminations coexisting with molybdenite in the quartz veins (Fig. 5c, d). Massive pyrite associated with minor Mo mineralization is regarded as the second type (Py2).

Stage III: The major Mo mineralization episode occurred in Stage III, which is dominantly represented by K-feldspar + quartz + molybdenite + pyrite veins (Fig. 4e, f). Pervasive K-feldspar alteration is extensively developed in the quartz veins. Pyrite occurs as irregular interstitial crystals bordered by molybdenite (Fig. 5e, f). Molybdenite occurs as fine-grained crystals and is closely arranged in discontinuous streaks showing rosette texture along the boundaries of K-feldspar + quartz + pyrite veins, or as disseminations throughout the K-feldspar + quartz + pyrite veins and altered wallrocks. Quartz is microcrystalline and commonly line vug. As indicated by the crosscutting relationships, the K-feldspar + quartz + molybdenite veins postdate the early barren veins and quartz + pyrite + molybdenite veins (Fig. 4e, f and 5e, f), but predate the late barren veins. These veins are also characterized by abundant polymetallic sulfides such as chalcopyrite, galena and sphalerite.

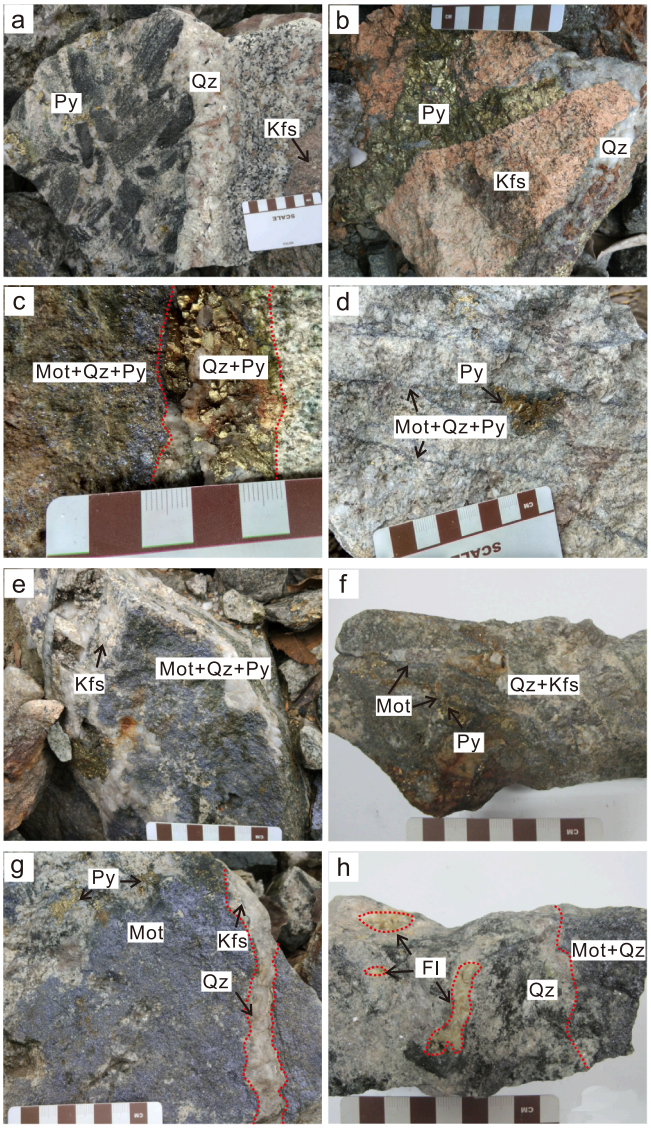

Fig. 4. Photographs (a–h) showing structures, textures, and mineralogy of ores from the Shapoling Mo deposit. (a) Early quartz cement surrounding wall-rock breccia; (b) barren quartz + pyrite vein as fracture fillings in potassic wall-rock; (c) the marginal early pyrite + quartz vein was intruded by the quartz + pyrite + molybdenite vein and enclosed by intensive hydrothermal alteration; (d) quartz + pyrite + molybdenite veins crosscutting the early coarse-grained pyrite aggregates; (e) representative quartz + pyrite + molybdenite + K-feldspar vein; (f) fragments of early pyrite + quartz veins included in the quartz + pyrite + molybdenite + K-feldspar vein; (g) late barren quartz + K-feldspar vein crosscutting the early coarse-grained quartz + pyrite + molybdenite aggregates; (h) representative quartz + pyrite + fluorite + K-feldspar vein. *Abbreviations:* Py, pyrite; Sp, sphalerite; Gn, galena; Ccp, chalcopyrite; Mot, molybdenite; Qz, quartz; Kfs, K- feldspar; Fl, fluorite.

Stage IV: Stage IV marks the waning of hydrothermal activity without any major metal deposition or with minor molybdenite and pyrite, but with extensive formation of fluorite in the barren quartz veins, and within geodes. Fluorite occurs as blocky masses, veins, or disseminations (Fig. 4g, h) in association with sericite and calcite.

4. Samples and analytical methods

A total of 22 hand specimens were collected from the ores and wall rocks belonging to different stages (Figs. 2 and 3) and polished into sections for petrographic study. Samples of the first stage I were

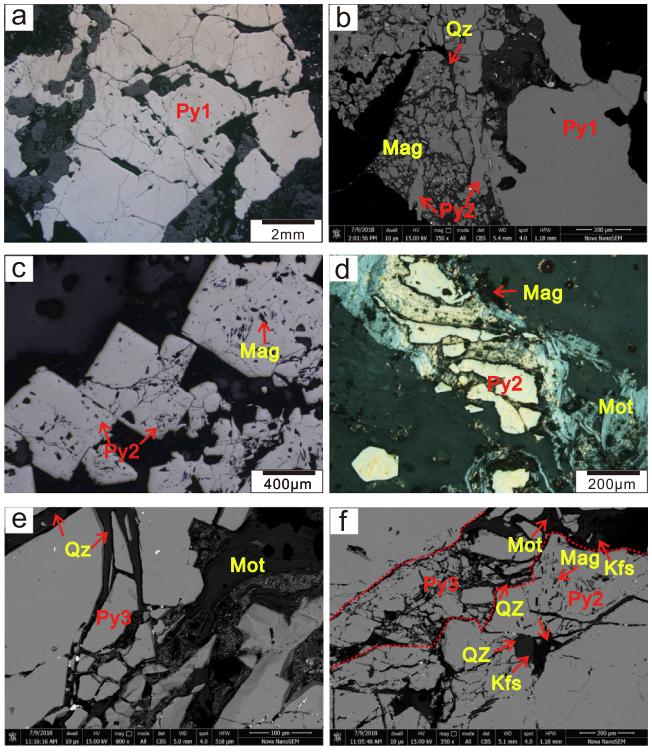

Fig. 5. Representative reflected light photomicrographs (a, c and d) and backscattered electron images (b, e and f) of pyrite from the Shapoling Mo deposit. (a) Representative pyrite grains from Py1. (b) Pyrite grains from Py2, quartz, and magnetite forming a vein partly replacing pyrite grains from Py1. Magnetite is present as inclusions in Py2. (c) Representative pyrite grains from Py2 in the quartz + pyrite vein. Magnetite is present as inclusions in Py2. (d) Representative pyrite grains from Py2 in the quartz + pyrite + molybdenite vein. (e) Pyrite grain from Py3 forms the irregular interstitial, and coexisting with curved, coarse grained flaky molybdenite aggregates. (f) Representative pyrite grains from Py3, molybdenite, K-feldspar, and quartz forming a vein crosscutting the Py2 + quartz + molybdenite vein. *Abbreviations:* Py, pyrite; Sp, sphalerite; Gn, galena; Ccp, chalcopyrite; Mot, molybdenite; Mag, magnetite; Qz, quartz; Kfs, K-feldspar.

collected from the potassic alteration zone of the deposit. A suite of samples from the last two stages (Stage II and Stage III) were obtained from the main orebody in the mine, representing a wide range of mineral assemblages. From these, nine representative samples were selected for pyrite trace element analysis using LA-ICP-MS technique and pyrite sulfur isotope analysis using SIMS technique. Three vein ore samples with quartz + pyrite (SPL-02, SPL-03 and SPL-09) belonging to Stage I, four stockwork – disseminated ore samples with molybdenite + quartz (SPL-04, SPL-05, SPL-08, and SPL-17) belonging to Stage II and two stockwork – disseminated ore samples with quartz + K-feldspar + molybdenite (SPL-16 and SPL-22) belonging to Stage III were used in this study. Polished sections were examined using transmitted and reflected light microscopy to document the types and textures of the pyrite. Selected polished sections were analyzed by FEI Nova NanoSEM 450 scanning electron microscope (SEM) equipped with an energy dispersive spectrometer (EDS), which enabled combined analysis of morphology and major element compositions of the various phases.

4.1. SIMS analysis

Two sample mounts were prepared by cutting 3 mm diameter pucks from polished sections using a cutter bar and mounted and casted in the central portion of a 25 mm diameter epoxy mount together with standard block. Standard blocks (cast separately to be reused) were made by mounting 1–2 grain fragments of pyrite. Care was taken to set the surfaces of the standard and sample blocks at the same level in the sample holder. Two sample mounts were trimmed to a thickness of 5 mm using a precision saw and then coated with 30 nm of gold.

In situ sulfur isotopic analyses (^{32}S, ^{33}S and ^{34}S) were measured using a CAMECA IMS1280 large-geometry ion microprobe at the Centre for Microscopy, Characterisation and Analysis, The University of Western Australia. The analytical set up and conditions, and data processing and error propagation applied to pyrite followed those described in LaFlamme et al. (2016) and Wang et al. (2017b). Instrumental mass fractionation was corrected through using the matrix matched standard Sierra pyrite ($\delta^{33}S$ = 1.09‰ and $\delta^{34}S$ = 2.17‰; LaFlamme et al., 2016, 2018). The 2σ uncertainty of $\delta^{34}S$ is 0.18‰, and the 2σ uncertainty of $\delta^{33}S$ is 0.19‰, based on the repeated measurements of internal reference material Sierra during the course of the analyses.

4.2. LA-ICP-MS analysis

Analytical instrumentation employed in this study comprises a Resonetics S-155-LR 193 nm excimer laser ablation system coupled to an Agilent 7700x quadrupole ICPMS, housed in the GeoHistory Facility (GHF), John de Laeter Centre, Curtin University, Perth, Australia. The methodology was described in detail by Wang et al. (2017c) and briefly introduced as below.

Depending on the pyrite size, analyses were carried by laser ablating spot diameters of 50 and 75 μm and at repetition rate of 7 Hz. The laser beam energy was maintained between 1.6 and 2.5 J cm^{-2}. Analytical time for each sample was 85 s, which includes 32 s of background measurement with laser off and 40 s of analysis with laser on. The laser ablation starts at 32 s and ends at 72 s. Tuning the flow rates for a ThO/Th ratio of < 0.5% minimized oxide polyatomic interferences. The sample cell was flushed with ultrahigh purity He (0.68 L min^{-1}) and N_2 (2.8 ml min^{-1}), and high purity Ar was employed as the plasma carrier gas. International glass standard GSD-1G was used as the primary reference material for the calculation of elemental concentrations, using stoichiometric ^{57}Fe as the internal standard element, and to correct for instrument drift. Standard blocks were run every 10 unknowns. Certified values (GeoReM: http://georem.mpch-mainz.gwdg.de/) for secondary standard BCR-2G treated as an unknown assuming 9.6385% Fe were reproduced to within 20% for most elements. A set of 24 trace elements (Ti, V, Cr, Mn, Co, Ni, Cu, Zn, Ga, Ge, As, Se, Mo, Ag, Cd, In, Sn, Te, Gd, W, Au, Pb, Ba, Bi) were measured from the pyrite on two sample mounts.

In this study, no attempt was made to remove the effects of micron sized inclusions on the pyrite. However, inspection of the LA-ICP-MS output traces from each laser spot analysis enables an estimation of whether a particular trace element occurs within a homogeneous invisible or nano-sized inclusion or as larger isolated micron-sized inclusions in the pyrite (Maslennikov et al., 2009; Zhang et al., 2014).

5. Results

5.1. Pyrite types and textures

Pyrite is the predominant sulfide mineral in Stage I, Stage II, and Stage III. Petrographic observations of polished sections and sample mounts define three main pyrite types from the Shapoling deposit, showing paragenetic sequences from Py1 to Py3:

The first type (Py1) is composed of coarse-grained subhedral to euhedral pyrite associated with few fine-grained inclusions of galena and chalcopyrite (Fig. 5a, b). Py1 widely occurs in the Stage I mineralization, where it forms disseminations of euhedral crystals (1–3 μm) in the wall rock and early barren quartz vein. Py1 is texturally homogeneous and rarely contains mineral inclusions. Structural overprint is indicated by cataclastic texture and differently oriented linear clusters

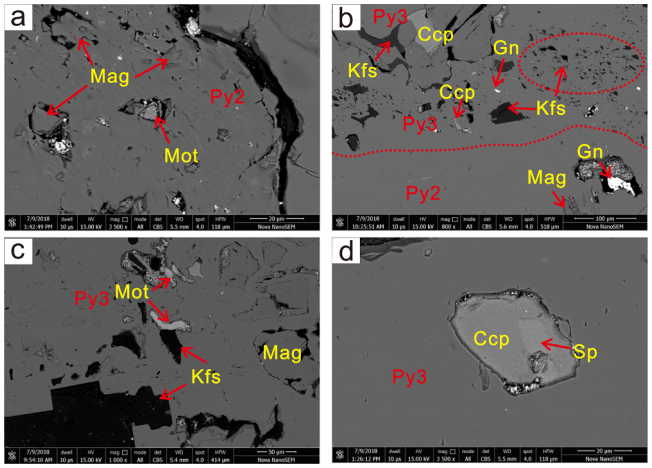

Fig. 6. Back-scattered electron images showing compositional zonation and mineral inclusions in three types of pyrite. (a) Molybdenite and magnetite inclusions in Py2. (b) Py3 overgrowth around Py2, showing porous textures and abundant inclusions of chalcopyrite, galena, and K-feldspar. (c) Molybdenite, K-feldspar and magnetite inclusions in Py3. (d) Chalcopyrite intergrown with sphalerite in Py3. *Abbreviations:* Py, pyrite; Sp, sphalerite; Gn, galena; Ccp, chalcopyrite; Mot, molybdenite; Mag, magnetite; Qz, quartz; Kfs, K-feldspar.

of Py2.

The second type (Py2) is observed as a component of metallic mineral assemblage, often in the form of subhedral-anhedral grains (50–300 μm) coexisting with molybdenite in quartz veins and cutting the wall rocks at Stage II. Py2 grains display jagged grain boundaries and form superimposed sporadic to dense disseminated molybdenite aggregates or oriented linear clusters among the quartz + molybdenite veins (Fig. 5b–d). Py2 is characterized by abundant magnetite inclusions and hosts numerous chalcopyrite, galena, and molybdenite grains differing from Py1 (Fig. 6a, b).

The third type (Py3) forms irregular interstitial, and vein-related pyrite with size of 50–150 μm (Fig. 5e, f). This pyrite type is preferentially enveloped by a hydrothermal vein assembly of molybdenite + quartz ± K-feldspar at Stage III. Py3 has overgrown Py2 and generally has porous textures and contains abundant inclusions of chalcopyrite, galena, sphalerite, K-feldspar and lesser molybdenite, quartz (Fig. 6b–d).

5.2. Trace element compositions of pyrite

A total of 109 pyrite LA-ICP-MS spot analyses were performed on various types of pyrite from the Shapoling Mo deposit. A total of 24 elements were analyzed: Ti, V, Cr, Mn, Co, Ni, Cu, Zn, Ga, Ge, As, Se, Mo, Ag, Cd, In, Sn, Sb, Te, Gd, W, Au, Pb, Bi. These data and their mean and range values are presented in Table 1, and the detailed data are available in Supplementary Table 1. Representative LA-ICP-MS time-resolved depth profiles for each type of pyrite recorded during spot analyses are shown in Fig. 6.

Among the analyzed elements, Co and Ni are abundant in pyrite with concentrations that are highly variable ranging from 0.06 ppm to 5800 ppm, and from 1.5 ppm to 769 ppm, respectively (Table 1). The flat and similar time-resolved depth profiles for Co, Ni and Fe prove the existence of Co and Ni in pyrites (Fig. 7). Ti, Cu, Zn, Te, Bi and Pb are also abundant elements in pyrite, with highly variable concentrations ranging from 3.9 ppm to 227 ppm, 0.04 ppm to 600 ppm, 0.13 ppm to 381 ppm, 0.12 ppm to 146 ppm, 0.0025 ppm to 279 ppm, and 0.01 ppm to 11400 ppm, respectively (Table 1). Measured values for Cu, Zn, Te, Bi and Pb vary over several orders of magnitude. Most of the higher concentrations (numerous spikes in Fig. 7a–c) can be attributed to inclusions of galena, chalcopyrite, sphalerite, Te- and Bi-compounds. Apart from these trace elements, significant Au contents were also detected in all pyrite samples (Supplementary Table 1). Gold shows mean value as high as 6.4 ppm, with one spot analysis reaching 70 ppm (sample SPL-16_13, Supplementary Table 1). The Au concentrations are relatively smooth in each pyrite type but display certain variations of an order of magnitude among pyrite grains in single samples (Supplementary Table 1). Time-resolved depth profiles for arsenic are flat (Fig. 7), but the concentrations of arsenic are low in most samples, suggesting that the pyrites at Shapoling are not As-bearing (Supplementary Table 1). Mo is also detected in the fractional pyrite grains and shows mean concentrations of 20.1 ppm, with one spot analysis reaching 180 ppm (Table 1). Numerous spikes of Mo are displayed in the time-resolved depth profiles (Fig. 7c), attributed to probable molybdenite inclusions. However, for sample SPL-16, the consistent concentrations and flat time-resolved depth profile possibly indicate incorporation of Mo as nanoscale inclusions but that those inclusions are very small and homogeneously distributed. Ge, As, Se, and Ag are detectable but are low in most analyzed pyrites, and range from high ppb-levels to a few hundreds of ppm (Supplementary Table 1). V, Cr, Mn, Ga, Cd, In, Sn, Sb, Gd and W are generally lower than the detection limit (Supplementary Table 1), and some samples show low abundance, with maximum concentrations of a few dozens of ppm as detected. The time-resolved laser ablation depth profiles (Fig. 7) indicate that the elevated concentrations of elements such as Pb, Zn, Cu, Te and Bi are directly related to small inclusions in many Py2 and Py3 grains, whereas Se and As follow the Fe signal in the Py1, Py2 and Py3 grains, indicating that these elements exist in the pyrite lattice or in inclusions of a size that cannot be resolved by the laser (submicrometer particles).

Elements such as Co, Ni, Cu, Zn, Mo, Ag and Pb show distinct trace signatures for each of the three pyrite types and are illustrated in the plots of Figs. 7 and 8. Py2 and Py3 possess higher ranges of Mo concentrations than Py1 (Table 1), and the highest mean value is observed in the Py2 (mean value up to 30 ppm), although most spots in Py3 contain higher Mo concentration than Py2, which might be due to the impact of high values of some single grains (Supplementary Table 1). The Ag contents for Py1, Py2 and Py3 are 0.01–9.5 ppm, 0.01–16.8 ppm, and 0.05–72 ppm, respectively (Table 1). The Py3 grains from the main metallogenic epoch have higher Au concentrations compared to Py1 and Py2 from other stages (Fig. 9, Table 1).

The coarse-grained euhedral pyrites (Py1) have lower Cu, Zn, Ag and Pb contents compared with those in Py2 and Py3. The Py3 from the main metallogenic epoch shows abundant concentration of Cu, Zn, Ag and Pb (Figs. 8a and 9). Compared to Py1 and Py2, the Py3 also contains higher trace element concentrations such as: Ti (5.1–227 ppm), As (0.58–149 ppm), Te (1.1–146 ppm) and Bi (1.5–279 ppm) (Table 1).

5.3. Sulfur isotope systematics

The complete sulfur isotopic dataset (n = 57) is provided in Supplementary Table 2, and the results are plotted in a $\delta^{34}S$ versus $\Delta^{33}S$ diagram (Fig. 10). The Py1 and Py2 exhibit negative ranges of $\delta^{34}S$ at −2.33‰ to −0.37‰ (± 0.15‰), and −2.29‰ to −0.5‰ (± 0.15‰), respectively (Table 2). The late Py3 is distinctly enriched in $\delta^{34}S$ (−2.55‰ to 1.48‰, ± 0.2‰) relative to other pyrite types (Fig. 10).

As a measure of mass-independent fractionation, the three types of pyrites have a tiny variation in $\Delta^{33}S$ values between −0.11 and 0.06 (Table 2), possibly suggesting a single sulfur source. Fig. 10 is utilized to extract information about the source of sulfur and the formation process that affected the pyrite. The observation of partial positive $\delta^{34}S$ coupled with tiny variation of slightly negative $\Delta^{33}S$, together with the observed isotopic gradient from Py1 to Py3 indicate a probable influence of changes in pH, H_2S:SO_4, or sulfur disproportionation during the evolution of ore-forming fluid (Ohmoto, 1986).

Table 1
Summary of distinguishing features of the characterizing trace element (ppm) in different type of pyrite.

	Py1 SPL-02, SPL-03, SPL-09		Py2 SPL-4, SPL-5, SPL-17		Py3 SPL-16, SPL-22		Total	
	Mean	Range	Mean	Range	Mean	Range	Mean	Range
Ti	4.6	3.9–8.6	12.2	4–136	31.9	5.1–227	15.3	3.9–227
V	1.1	0.02–15.2	1.3	0.02–9.0	7.1	0.03–44.4	3.8	0.02–44.4
Cr	0.25	0.18–0.33	0.43	0.18–1.2	1.4	0.19–4.0	0.98	0.18–4.0
Mn	104	1.1–880	49.6	1.4–358	91.1	1.6–1220	81.5	1.1–1220
Co	23.2	0.06–615	259	0.51–5800	175	21.7–597	164	0.06–5800
Ni	188	7.3–769	38.3	1.5–493	80.3	10.3–317	95	1.5–769
Cu	3.1	0.04–22.7	0.98	0.04–10.1	50.3	1.4–600	16.7	0.04–600
Zn	5.9	0.13–98	4.7	0.13–44.4	29.5	0.31–381	15.1	0.13–381
Ga	1.0	0.02–7.0	0.55	0.02–2.3	1.4	0.02–8.6	1.1	0.02–8.6
Ge	8.2	7.7–8.9	8.3	7.4–8.9	8.3	7.5–9.2	8.3	7.4–9.2
As	5.4	0.08–26.2	4.8	0.46–15.4	22.8	0.58–149	9.9	0.08–149
Se	15.9	8.6–29.8	9.9	2.1–41.8	3.2	1.5–5	9.9	1.5–41.8
Mo	0.16	0.01–0.74	30	0.02–178	19.7	0.01–180	20.1	0.01–180
Ag	0.66	0.01–9.5	0.79	0.01–16.8	9.5	0.05–72	3.3	0.01–72
Cd	0.05	0.02–0.11	0.11	0.02–0.31	0.61	0.03–2.3	0.41	0.02–2.3
In	0	0–0	0.01	0–0.04	0.02	0–0.05	0.01	0–0.05
Sn	0.02	0.01–0.02	0.05	0.01–0.17	0.28	0.03–0.65	0.16	0.01–0.65
Sb	0.05	0.02–0.14	0.12	0.01–0.57	0.16	0.02–0.66	0.11	0.01–0.66
Te	6.1	0.15–42.8	15	0.12–128	59	1.1–146	25.3	0.12–146
Gd	0.05	0.01–0.08	0.01	0.01–0.01	0.88	0.01–4.6	0.60	0.01–4.6
W	0.54	0.01–1.6	0.03	0.01–0.08	10.1	0.02–104	6.8	0.01–104
Au	5.3	0.42–32	4.6	0.04–35	10.1	0.67–70	6.4	0.04–70
Pb	67.6	0.01–1220	99.5	0.01–1630	1175	3.8–11400	423	0.01–11400
Bi	9.3	0–77	4.6	0.01–46	55.2	1.5–279	22.3	0–279
Co/Ni	0.75	0–22.5	71.3	0.005–1973	3.3	0.1–12.8		

6. Discussion

6.1. Trace element characteristics of pyrite

Pyrite is a ubiquitous sulfide phase in most hydrothermal systems, and its precipitation can effectively control the partitioning of a wide array of trace elements of economic and environmental importance, such as Au, Ag, As and other heavy metals (Deditius et al., 2008; Large et al., 2009). Previous studies have indicated that trace elements in pyrite may occur in several ways: (1) as structurally bound elements (i.e., as solid solution within the crystal lattice (Reich et al., 2013), (2) within invisible nanoparticles of sulfides (Ciobanu et al., 2012), (3) as micro- to nanosized mineral inclusions (Thomas et al., 2011). In assessing the results from our study, the first step is to evaluate the distribution and concentration of various trace elements which are controlled by micro- to nanoscale inclusions, invisible solid solution or nanoparticles in the pyrite lattice.

(1) Though there is visible abundance of microscale mineral inclusions and vugs within pyrite in reflected light (Fig. 6), the time-resolved depth profiles for Co, Ni, As and Te are generally smooth and consistent with Fe (Fig. 7), indicating that these siderophile and chalcophile elements are commonly distributed in different pyrite types via isomorphism. Ni and Co are incorporated into the pyrite lattice via isomorphous replacement of Fe, whereas As, Se and Te enter the lattice through replacing S.
(2) Due to ionic size, lead has a faster precipitation rate from an aqueous solution as metal sulfide when compared to Fe (Koglin et al., 2010; Zhao et al., 2011). Thus, Pb forms galena prior to the formation of pyrite, and galena inclusions in pyrite are common. The Pb, Zn and Cu concentration of pyrite are characterized by variable contents ranging from below lower limit of detection to several thousands of ppm (Supplementary Table 1). We interpret that Pb, Zn and Cu are primarily distributed in pyrite as invisible or visible galena, sphalerite and chalcopyrite inclusions. The observed higher levels of Pb, Zn and Cu in porous, fractured or inclusion-rich pyrite support this contention (Fig. 6a–d). The correlations between Ag, Pb, Bi and Sb (Fig. 8a, c, f) indicate that most Ag occurs as solid solution or inclusion of Sb- or Bi-compounds (e.g. argyrythrose, matildite) in galena (Cook et al., 1998; Zhao et al., 2011; Zhang et al., 2014), in addition to native Ag. The Cu vs Ag plot (Fig. 8d) shows prominent positive correlation among Ag and Cu which further confirms the silver can be incorporated into chalcopyrite to form argentiferous chalcopyrite via Ag–Cu solidstate exchange reaction (Li et al., 2016).
(3) The major ore-forming elements are Mo and minor Au in the Shapoling Mo deposit. We note, however, that porous or fractured domains often contain higher levels of trace elements. Fractured pyrite also contains higher Mo concentration as shown in Fig. 9b. Since Mo-bearing inclusions (e.g. molybdenite) were observed mainly in Py2 and Py3, we suspect that higher Mo concentrations in the porous or fractured pyrite are caused by collateral ablation of minute or submicroscopic inclusions located in the micro-fissures of pyrite. Gold was probably not incorporated into the pyrite lattice but formed as minute or submicroscopic inclusions of discrete Au-bearing phases within pores and interstices of the porous pyrite in all the samples. Therefore, high Mo and Au concentrations probably resulted from inclusions of molybdenite and gold, respectively. In conclusion, the distribution and concentration of most trace elements, such as Mo, Au, Pb, Zn, Ag and Cu, are likely controlled by mineral micro/nano-inclusions. Co, Ni, As, Se and Te are the only elements analyzed in this study that are incorporated in the pyrite structure, rather than mineral micro/nano-inclusions.

6.2. Genesis of pyrite

Studies on the trace element chemistry and sulfur isotopic composition of pyrite can be used to estimate the origin of pyrite and to characterize the genesis of hydrothermal ore deposits (Bajwah et al., 1987; Cook et al., 2009a,b, 2011; Reich et al., 2010; Deditius et al., 2011).

Nickel can easily enter the lattice via isomorphous replacement of

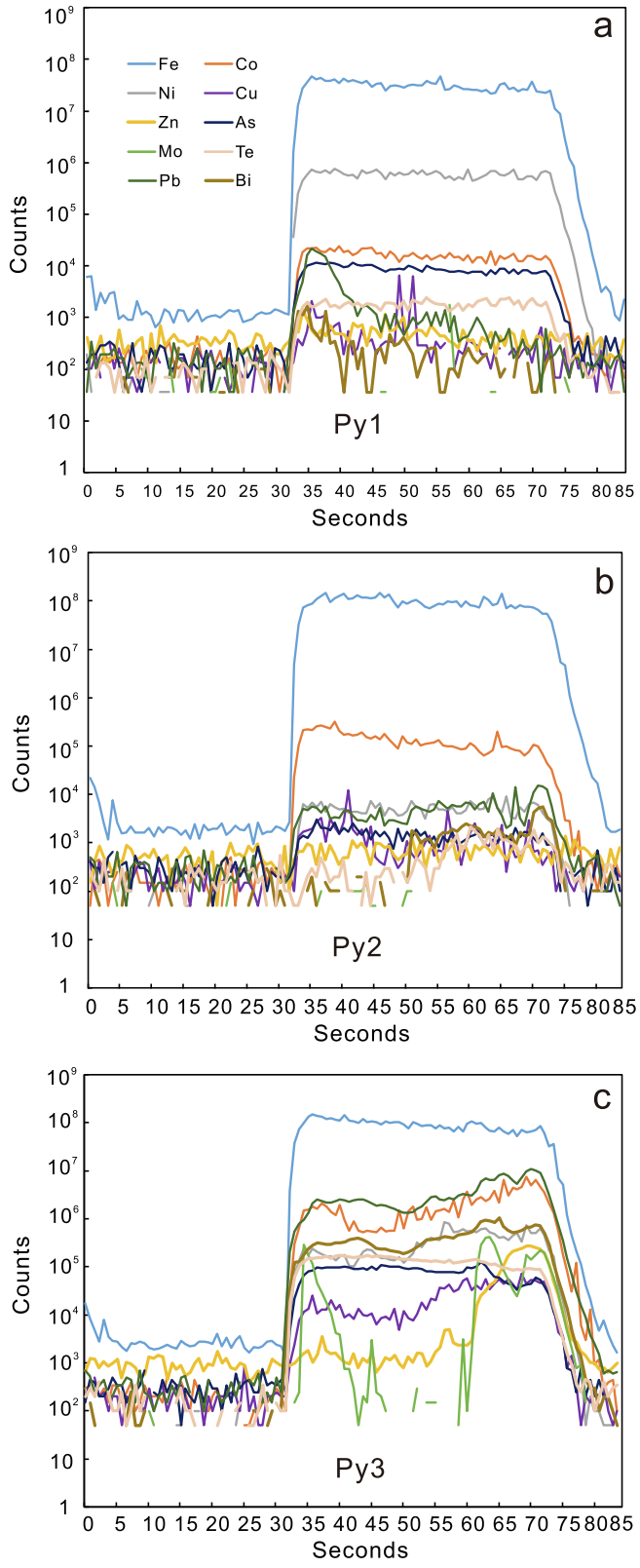

Fig. 7. Representative LA-ICP-MS time-resolved depth profiles for different pyrite types from the Shapoling deposit. (a) Py1: note the relative high counts of Ni, Co, As, and Te, and low counts of Cu, Zn and Pb; (b) Py2: high counts of Co, Pb and Ni. Note the profiles for Pb is parallel with Fe; (c) Py3: note the high counts of Pb, Co, Bi, Ni, Te, As, Cu, Zn and Mo, the profiles for most elements are unstable except the profile for As and Te. The spikes in the profiles for Au, Pb, Zn, Cu and Mo indicate micro inclusions of these metals.

Fe, and is not readily released during the recrystallization of hydrothermal pyrite (Huerta-Diaz and Morse, 1992; Morse and Luther Iii, 1999; Tribovillard et al., 2006; Large et al., 2009; Koglin et al., 2010). The Ni distribution patterns in pyrite can provide information for the pyrite-precipitating fluid, the chemistry of which is controlled by its primary composition and modification via wall rock/fluid interaction (Zhao et al., 2011). Ultramafic and mafic rocks are strongly enriched in Ni (such as the mean Ni concentration of mantle-derived rock is 2200 ± 500 ppm, Palme and O'Neill, 2003); in contrast, felsic rocks usually contain low Ni concentrations. The Ni concentrations of continental crust range between 19 and 60 ppm (Rudnick and Gao, 2003). Therefore, pyrite from granite-related deposits is expected to contain negligible Ni. In the Shapoling Mo deposit, Ni concentrations of pyrite range from 1.5 ppm to 769 ppm (on average 95 ppm, Table 1) that is higher than Checangyu Mo deposit in the Xiaoqinling district which shows typical source of ore-forming materials from felsic rocks (Zhao et al., 2015) but lower than Ni concentrations of pyrite (on average 800 ppm) from main metallogenic stage of Au deposits in the Xiaoqinling district which indicates a mafic or ultramafic provenance (Zhao et al., 2011). This possibly indicates that the pyrite and the source material were mainly derived from felsic rocks with significant contribution from the mantle.

The pyrites of different types in this study show some similarities and differences in element compositions and sulfur isotope values. The $\delta^{34}S$ isotope compositions of pyrites are associated with oxidation state of fluids (Ohmoto, 1979; Neumayr et al., 2008), suggesting that oxidation state plays a major role in Mo mineralization. The pyrite as the dominant sulfide phase in the Shapoling deposit shows relatively negative $\delta^{34}S$ values (mean −1.09‰), suggesting oxidized conditions (Neumayr et al., 2008). Based on the presence of redox-indicative mineral assemblages such as magnetite and limonite, we suggest the proximal phengitic zone represents relatively oxidized fluids.

The slight difference in the range of $\delta^{34}S$ between different pyrite types (Fig. 10) can be easily explained. We interpret the variation in the $\delta^{34}S$ of early pyrite as a record of $\delta^{34}S$ variability in the parental fluid during deposition from magmatic fluid. The variation in the parental fluid at Shapoling is most likely caused by changes in sulfur speciation during the phase separation of magmatic fluid. It is possible that the shift to more positive $\delta^{34}S$ values within Py3 may reflect the changes of pH, temperature, sulfur fugacity and oxygen fugacity during chemical reactions between the magmatic fluid and the wall rock along the fracture, and/or progressive mixing with meteoric water (Ward et al., 2017).

Price (1972) noted that the Co/Ni ratio of hydrothermal pyrite is highly variable and is typically > 1, whereas the Co/Ni ratio for sedimentary pyrite is < 1, with 0.63 as the typical value. However, numerous hydrothermal pyrites also have Co/Ni ratios of less than 1.0, thus low Co/Ni ratios are not necessarily indicative of syngenetic pyrite (Price, 1972). Hence, the Co/Ni ratio applied for classification and discrimination should be considered in the context of geological evidence (Bralia et al., 1979). The Co/Ni ratios of Py1 range 0.0004–22.5 (Table 1), excluding an unusually high value 22.5, with an average of 0.07. However, the Py1 formed in early Stage I has negative $\delta^{34}S$ values (range −2.33 to −0.37‰, mean −1.12‰), which is closely associated with magmatic hydrothermal activity. In contrast, the Co/Ni ratios of Py2 and Py3 range 0.005–1973 (mean = 71.3) and 0.1–12.8 (mean = 3.3), with only several values below 1 (Supplementary Table 1; Table 1), comparable to magmatic hydrothermal pyrite and well consistent with Py1. The Py1 usually contains higher Ni than those in Py2 and Py3, probably indicating the changes of temperature and pressure which lead to increased leaching of Ni from the source area. Similarly, Py1 usually co-exists with galena and chalcopyrite; the changes in temperature and pressure might have caused more Pb and Cu to be precipitated from the ore-forming fluid (Zhao et al., 2011).

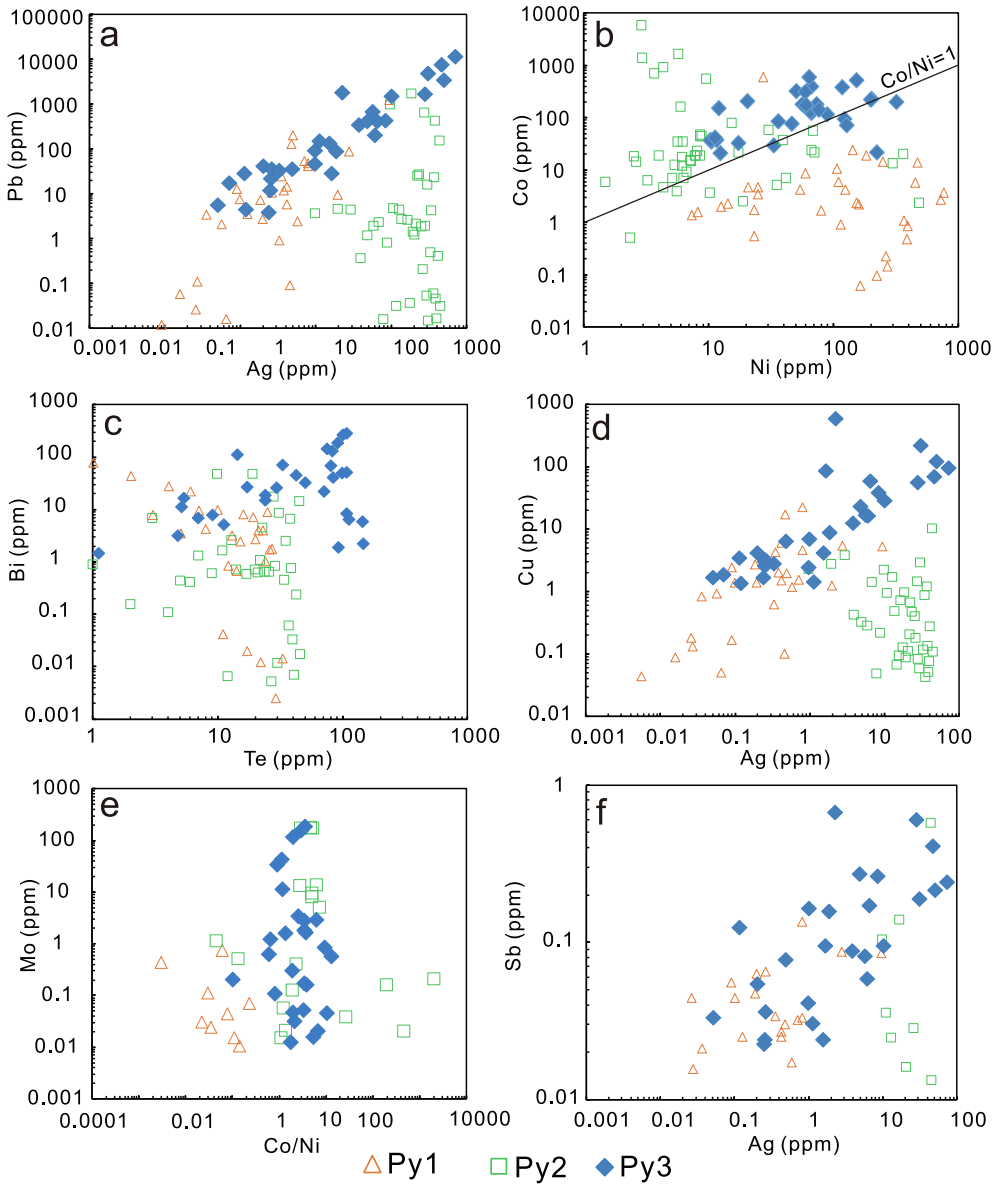

Fig. 8. Binary plots of (a) Pb vs. Ag, (b) Ni vs. Co, (c) Bi vs. Te, (d) Ag vs. Te, (e) Mo vs. Co/Ni and (f) Sb vs. Ag for different pyrite types. The trace element concentrations are from Supplementary Table 1, and all measurements below minimum detection limit are discarded.

6.3. Implications for ore genesis

The $\delta^{34}S$ values of the pyrites range between −2.55 and 1.48‰, largely clustering between −2.5 and 0‰ (mean = −1.09‰), and showing a prominent normal distribution (Fig. 11). The narrow range of sulfur isotopic composition of the pyrites indicates that the sulfur might have originated directly from a magmatic system or indirectly from leaching or desulphidation of primary magmatic sulfide minerals (Chen et al., 2009; Wang et al., 2014a,b, 2018). Compared with $\delta^{34}S$ values of volcanic rocks of the Xiong'er group (average of 4.1‰), metamorphic rocks of the Taihua group (average of 3.2‰) and Huashan pluton (average of 3.0‰), the ores from the Shapoling Mo deposit tend to have slightly lower $\delta^{34}S$ values. Considering that fractionation is caused by variations in physico-chemical conditions, these geological formations as possible sulfur sources cannot be precluded in spite of the discrepancies of $\delta^{34}S$. Compared with the Leimengou porphyry Mo deposit ($\delta^{34}S$ values cluster at 1.8‰–2.6‰, with an average of 1.27‰; Chen et al., 2014a) and Qiyugou breccia pipe-hosted gold deposit ($\delta^{34}S$ values cluster at −1 to 1‰, with an average of −0.2‰; Chen et al., 2009) around the Huashan pluton (Fig. 1), the Shapoling Mo deposit shows slightly lower $\delta^{34}S$ values than the Leimengou Mo deposit, and are similar to the Qiyugou gold deposit. From the porphyry type Leimengou Mo deposit to breccia pipe-hosted type Qiyugou gold deposit, and to vein-type Shapoling Mo deposit, the average $\delta^{34}S$ values change from +1.27‰, to −0.2‰ and to −1.15‰. These trends suggest a homogenous sulfur source and evolutionary trend, implying magmatic control on the mineralization event (Fig. 11).

Previous SHRIMP, LA-ICP-MS, and TIMS zircon U-Pb age data, together with K-feldspar K-Ar and amphibole Ar-Ar ages from the ore-related granitic plutons in the northern part of the Xiong'ershan ore district are compiled in Fig. 12a. These data show that the ages of the ore-related intrusions cluster into three magma pulses: 166–153 Ma, 151–140 Ma, and 138–126 Ma (Fig. 12a). The first pulse of magmatic activity (166–153 Ma) is represented by the Wuzhangshan granitic pluton and the quartz porphyry phase of the Qiyugou deposit. The second magmatic activity (150–141 Ma) formed the ore-bearing porphyry of the Leimengou deposit and part of the Huashan pluton, which is widely exposed in the mining area. The last pulse of magmatism (138–126 Ma) generated the main body of the Huashan pluton and major ore-bearing porphyries in the Leimengou deposit and Qiyugou

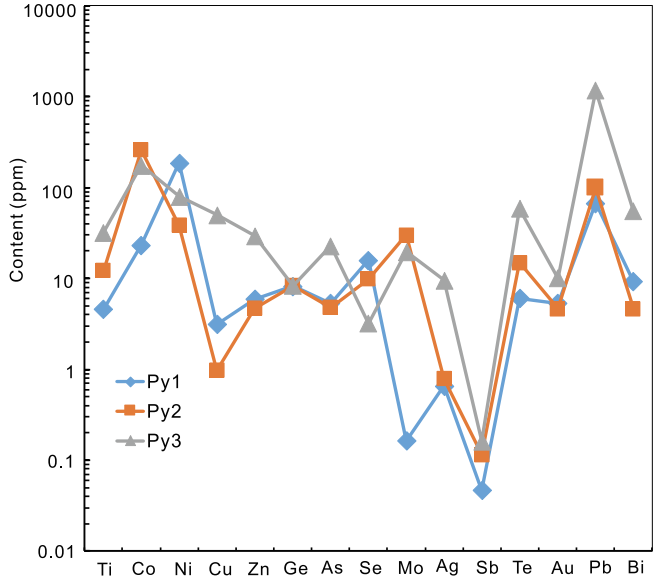

Fig. 9. Diagrams showing the mean concentrations of selected trace elements in different types of pyrite.

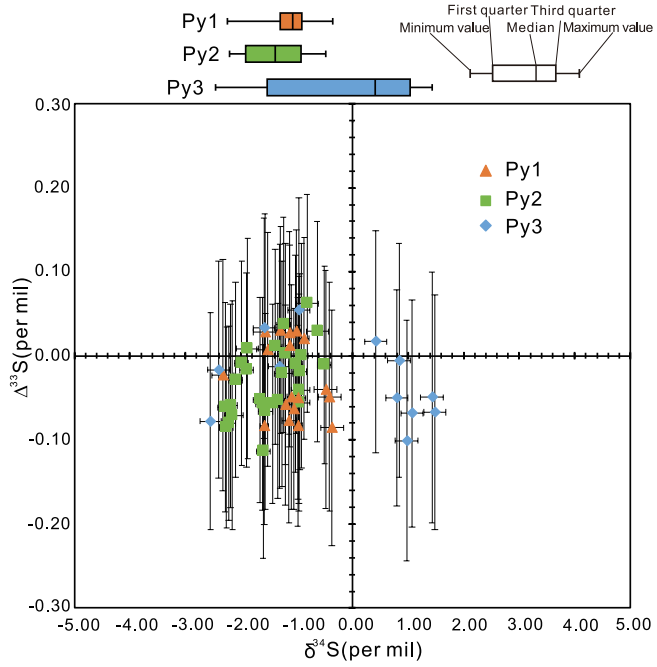

Fig. 10. Diagram showing the sulfur isotope ($\delta^{34}S$ and $\Delta^{33}S$) as determined by in situ analysis with an ion microprobe in different types of pyrite. Error crosses are the overall uncertainty (at the 2SD level) based on propagating the individual analysis repeatability with the reproducibility for the relevant analytical session. For each sample, the 25–75 percent quartiles are drawn using a box. A box and whisker plot at the top shows the variation in $\delta^{34}S$ between the different pyrite types. The median is shown with a horizontal line inside the box. The minimal and maximal values are shown with short horizontal lines ("whiskers").

deposit, which also correspond to the most extensive and important metallogenic events of gold and Mo deposits in the Xiong'ershan ore district (Deng et al., 2014a). The Re-Os model ages of the molybdenite from the Leimengou porphyry type Mo deposit, Qiyugou breccia pipe-hosted gold deposit and Shapoling vein-type Mo deposit bracket their emplacement ages in the range from 139 Ma to 130 Ma (Fig. 12b–d), which is close to the last pulse of igneous activity (138–126 Ma) in the Xiong'ershan district (Fig. 12a).

Based on a comparison of the Re content in the molybdenite and comprehensive studies from different types of endogenic Mo deposits, Mao et al. (1999) and Stein et al. (2001) proposed that the Re content of molybdenite remarkably decreases from the mantle source and/or subducted oceanic slab to the crustal source. Ore deposits that involve significant mantle materials and/or subducted oceanic slab can be expected to show overall higher rhenium concentrations (generally > 100 ppm) in the associated molybdenite. In contrast, ore deposits originated from continental crustal rocks or organic-poor sedimentary sequences generally have lower rhenium concentrations in the associated molybdenite (generally < 50 ppm) (Mao et al., 1999; Stein et al., 2001; Deng et al., 2016). The Shapoling Mo deposits are characterized by higher concentration of rhenium in the molybdenite, ranging from 147 to 307 ppm (Su et al., 2009; Liu et al., 2011), which are comparable with those in the Qiyugou gold deposit (Re = 19.25–521.96 ppm, mean = 406.85 ppm, Yao et al., 2009). The above Re contents are also comparable with those in the Huangshui'an Mo deposit (Re = 60.1–138 ppm; Cao et al., 2014) and Huanglongpu Mo deposit (Re = 256.0–633.1 ppm; Huang and Du, 1994; Stein et al., 1997), which are associated with carbonatite dykes reflecting mantle source. It is possible that the Huashan pluton was mainly derived from the melting of ancient crustal components of the Taihua Group basement with significant contribution from the mantle or juvenile crust (Xiao et al., 2012).

Therefore, the Mo mineralization of the Shapoling Mo deposit and the regional Mo and Au mineralization (139–130 Ma) are possibly identical and share similar mantle-related signature. In addition, there is a close relationship between the contemporaneous magmatic activity and the Shapoling deposit in the Xiong'ershan ore district associated with the Early Cretaceous magmatic-hydrothermal mineralization events that resulted from lithospheric thinning, asthenospheric upwelling and partial melting of the lower crust in a vast area of East China (Mao et al., 2008, 2010, 2011; Zhang et al., 2017).

6.4. Implications for ore-forming process

The variation of trace elements (such as Co and Ni) hosted in solid-solution and sulfur isotopic composition reflect the variation in chemical composition of hydrothermal fluids during the continuous growth of pyrite (Ulrich et al., 2011; Reich et al., 2013; Tanner et al., 2016). Based on textural features, trace element chemistry and sulfur isotopic composition of the three pyrite types, we propose the ore-forming process as below.

(1) During 138–126 Ma, fault-controlled emplacement of magmas generated the plutons, stocks and dikes in various scales. The Py1 was formed during the subsequent magmatic hydrothermal activity. The Py1 formed at the early Stage I with Co/Ni ratios < 1 and $\delta^{34}S$ values < 0‰ (Tables 1 and 2), suggesting precipitation from high temperature magmatic ore-forming fluid. The coarse-grained euhedral pyrite (Py1) carries less fine-grained inclusions of galena and chalcopyrite than Py2 and Py3 (Figs. 5a, 6, 7a and 13a) owing to the higher temperature and slower growth rate, which allow the trace elements to be partitioned into separate mineral phases rather than pyrite in solid solution or as tiny inclusions (Butler and Rickard, 2000; Large et al., 2009).

(2) The Mo mineralization formed at 128.1 ± 7.1 Ma (Su et al., 2009; Liu et al., 2011), which is contemporaneous with the igneous activity (138–126 Ma) in the Xiong'ershan district (Fig. 12a). The Py2 along with molybdenite gradually grew from magmatic hydrothermal fluid during the upward migration of the hydrothermal fluid accompanied by decrease of temperature. The Py2 shows Co/Ni ratios > 1 and $\delta^{34}S$ values < 0‰, with anhedral texture and oriented linear clusters among the quartz + molybdenite veins (Figs. 5d and 13b). Py2 usually contains higher Mo, Cu, Pb, Zn and Ag concentrations than Py1 (Tables 1 and 2). The process resulted

Table 2
Summary of distinguishing features of trace element and sulfur isotope (‰) trends in different types of pyrite.

	Py1 SPL-02, SPL-03, SPL-09		Py2 SPL-4, SPL-5, SPL-17		Py3 SPL-16, SPL-22		Total	
	Mean	Range	Mean	Range	Mean	Range	Mean	Range
$\delta^{33}S$	−0.60	−1.22 to −0.26	−0.79	−1.25 to −0.27	−0.11	−1.39 to 0.70	−0.59	−1.39 to 0.7
2σ	0.12	0.10–0.16	0.12	0.1–0.16	0.16	0.16–0.17	0.13	0.1–0.17
$\delta^{34}S$	−1.12	−2.33 to −0.37	−1.48	−2.29 to −0.5	−0.15	−2.55 to 1.48	−1.09	−2.55 to 1.48
2σ	0.15	0.12–0.20	0.15	0.12–0.20	0.20	0.19–0.20	0.16	0.12–0.2
$\Delta^{33}S$	−0.03	−0.09 to 0.03	−0.03	−0.11 to 0.06	−0.03	−0.1 to 0.05	−0.03	−0.11 to 0.06
2σ	0.13	0.12–0.14	0.12	0.12–0.14	0.14	0.13–0.15	0.13	0.12–0.15

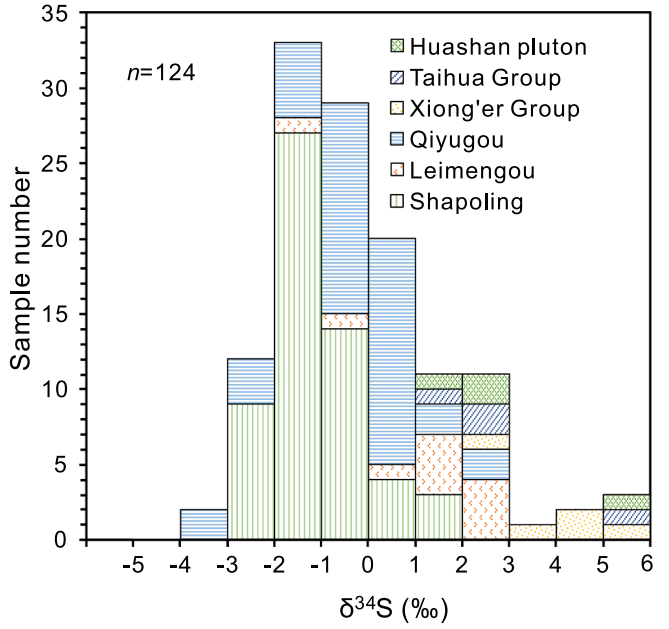

Fig. 11. Frequency histogram of $\delta^{34}S$ (n = 124) from the Huashan pluton (Chen et al., 2004), Taihua Group (Chen et al., 2004), Xiong'er Group (Chen et al., 2004), Leimengou Mo deposit (Chen et al., 2014a), Qiyugou gold deposit (Fan et al., 1994; Gao and Luan, 1994), and Shapoling Mo deposit (this study).

in incorporation of trace elements (such as Mo, Cu, Pb, Zn and Ag) into pyrite as tiny inclusions (Fig. 5f).

(3) Finally, the pyrite formed in late Stage III is irregular interstitial, containing elevated $\delta^{34}S$ values and negative Co/Ni ratios (Tables 1 and 2). The Py3 in this stage is usually most enriched in trace elements such as Mo, Cu, Pb, Zn and Ag (Figs. 6b–d, 7c and 13c). The irregular interstitial texture and abundant inclusions of Mo, Cu, Pb, Zn and Ag in Py3 indicate that the hydrothermal fluid experienced a rapid cooling process resulting in the precipitation of pyrite. Moreover, the shift to more positive $\delta^{34}S$ values within Py3 might have resulted from changes of sulfur fugacity and oxygen fugacity when chemical reactions occur between the magmatic fluid and the wall rock along fracture array (Ward et al., 2017). Analyses of fluid compositions, fluid salinities, $\delta^{18}O$ and δD from quartz at the coeval Leimengou Mo deposit (Chen et al., 2014a) and Qiyugou gold deposit (Chen et al., 2009) show that the hydrothermal fluids in this region were dominantly of magmatic origin, with minor mixing of meteoric water during the middle-late stage. Thus, it is reasonable to assume that the Py3 from the Shapoling deposit was also formed by mixing of fluids from magmatic and meteoric sources. The magmatic hydrothermal fluid circulated in host rocks with fluid-rock reactions have caused extensive potassic alteration in quartz veins and host rocks (Fig. 4e, f). The chemical evolution of hydrothermal fluid resulted in massive molybdenite precipitation. Hence, Stage III became the main metallogenic period.

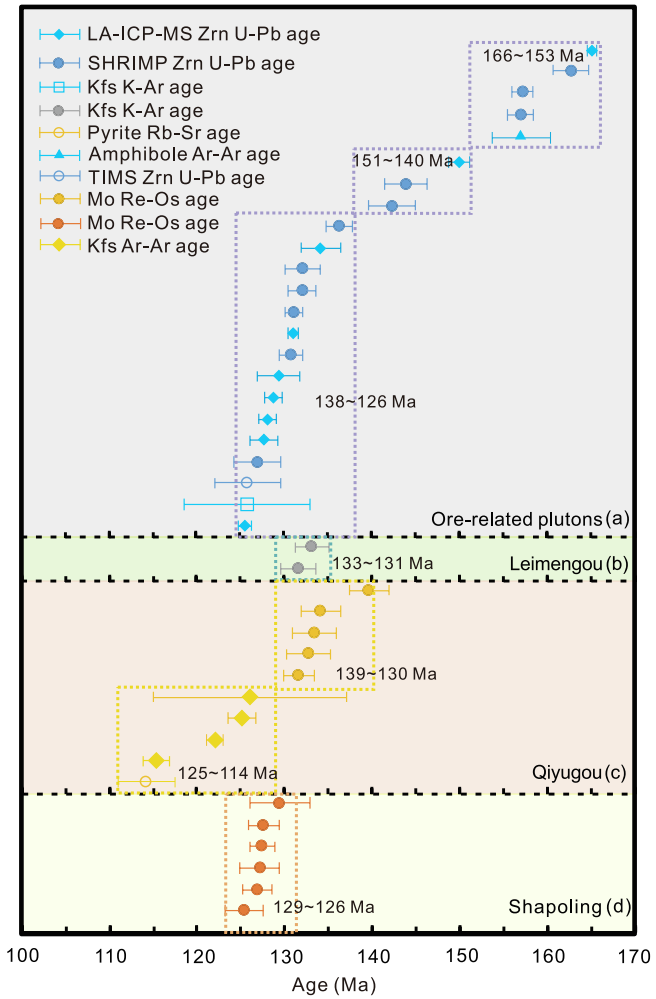

Fig. 12. Age distributions of the ore-related plutons (a), Leimengou Mo deposit (b), Qiyugou gold deposit (c), and Shapoling Mo deposit (d). Age data: ore-related plutons (Ren et al., 2001; Li, 2005; Li et al., 2006; Han et al., 2007a; Yao et al., 2009; Mao et al., 2010; Xiao et al., 2012; Cao et al., 2014; Deng et al., 2014a); Leimengou Mo deposit (Li et al., 2006); Qiyugou gold deposit (Wang et al., 2001; Han et al., 2007b; Yao et al., 2009); Shapoling Mo deposit (Su et al., 2009; Liu et al., 2011). *Abbreviation:* Kfs: K-feldspar; Zrn: zircon.

6.5. Implications for mineralization and mineral exploration

The abnormally high Mo concentrations in Py2 and Py3 probably resulted from nanoscale minerals or inclusions of molybdenite, which

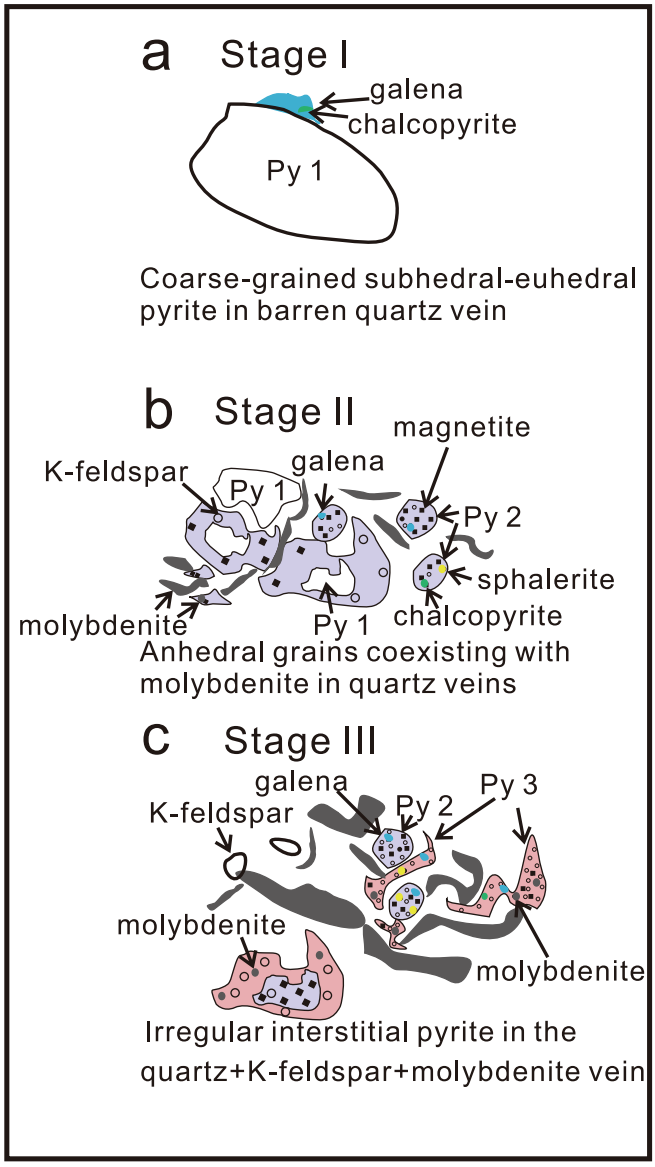

Fig. 13. Schematic textural evolution of pyrite and mineral assemblage from the Shapoling Mo deposit.

record a chronological history of cyclical metal saturation in the parent fluid. Mo-rich inclusions in both Py2 and Py3 pyrite grains exhibit (Fig. 6a, c), suggest cyclical saturation of Mo minerals. It is interesting that the early pyrite crystals (Py1) lack Mo-rich inclusions during the early barren stage, displaying a remarkable difference from Py2 and Py3. Hence, we propose that the Mo-bearing pyrites were formed together with the Mo mineralization. Therefore, we suggest that the Mo-bearing pyrite could be used as a pathfinder to prospect for high-grade Mo mineralization. Determination of the absolute Mo content of the pyrite would be required to assess the prospectivity of pyrite crystals.

In this study, the trace element chemistry and sulfur isotopic composition of pyrite in the vein-type Mo Shapoling deposit mainly indicate a magmatic origin. The early Cretaceous mineralization ages from the Shapoling Mo deposit coincide with the last pulse of the emplacement of the Huashan pluton, indicating a unified Early Cretaceous magmatic-hydrothermal event. Therefore, we infer that the Huashan pluton might have provided the source of ore-forming materials and has genetic link with the Mo mineralization. In this case, there is good prospect for the exploration of Mo mineralization around the inner and outer contact zones of the Huashan pluton.

7. Conclusion

(1) Three types of pyrites are identified in the Shapoling Mo deposit: Py1 is composed of coarse-grained euhedral pyrite in the wall rock and early barren quartz vein, Py2 as subhedral-anhedral grain coexists with molybdenite in quartz veins, Py3 forms the irregular interstitial pyrite in the quartz + K-feldspar + molybdenite dominated veins. Analytical result shows that Mo, Au, Pb, Cu, Zn and Ag from the pyrites occur mainly as invisible or visible inclusions. Py2 and Py3 possess higher Cu, Mo, Ag, Zn, Sb, Te, Pb and Bi concentrations than Py1. The Py1 and Py2 exhibit negative range of $\delta^{34}S$ at −2.33‰ to −0.37‰, while the Py3 is distinctly enriched in $\delta^{34}S$ (−2.55‰ to 1.48‰) relative to other pyrite types. Mo is enriched in Py3, suggesting that the Mo mineralization was mainly related to the intrusive rocks and magmatic fluids. By Combining the markedly high contents of rhenium (147–307 ppm) and geochronological data, the Shapoling deposit is considered to be genetically related to the Early Cretaceous magmatism.

(2) The analytical results indicate that the growth of coarse-grained Py1 is slower than Py2 and Py3 owing to higher temperature at early Stage I. Py2 along with molybdenite formed gradually from magmatic hydrothermal fluid accompanied by decrease in temperature during the upward migration of the ore-forming fluid. Finally, at late Stage III, the fluid-rock reaction and rapid cooling process caused the precipitation of massive molybdenite and Py3.

(3) Our results suggest that the Mo-bearing pyrite could be used as a pathfinder in Mo deposits to target high-grade Mo mineralization. We predict that more Mo mineralization might occur around the inner and outer contact zones of the Huashan pluton.

Acknowledgments

We are grateful to Prof. Franco Pirajno (Editor-in-Chief), Dr. Christiana Ciobanu (Associate Editor) and three anonymous reviewers for their constructive comments and suggestions which are very helpful to improve the quality of the manuscript. This study was jointly supported through the National Key Research and Development Program of China (2016YFC0600504), the Fundamental Research Funds for the Central Universities (2652017276 and 2652017218). LA-ICP-MS analysis were measured in the GeoHistory Facility at Curtin University which were funded via an Australian Geophysical Observing System (AGOS) grant provided to AuScope by the AQ44 Australian Education Investment Fund and SIMS analyses were measured at Centre for Microscopy, Characterisation and Analysis at the University of Western Australia which were funded via the Australian Microscopy and Microanalysis Research Facility, AuScope, the Australian Science and Industry Endowment Fund, and the State Government of Western Australia. Heejin Jeon, Brad McDonald and Noreen Evans is thanked for their technical support in running SIMS and LA-ICP-MS, respectively. We thank the team members from the China University of Geosciences Beijing for their field support.

Appendix A. Supplementary data

Supplementary data to this article can be found online at https://doi.org/10.1016/j.oregeorev.2018.12.019.

References

Bai, F.-J., Xiao, R.-G., 2009. Geologic characteristics and metallogenic prognosis of potassium feldspa quartz vein-type molybdenum deposits in Songxian county of Henan province, China. Molybdenum Ind. 33 (2), 19–32 (in Chinese with English Abstract).

Bai, F.-J., Xiao, R., Liu, G., 2009b. Genesis of k-feldspar-quartz vein type molybdenum deposit in Songxian county, Henan. Geol. Explor. 45 (4), 335–342 (in Chinese with English Abstract).

Bai, F.-J., Zhao, T.-P., Xiao, R.-G., Liu, G.-Y., 2010. Ore-forming fluid geochemistry of the k-feldspar quartz-vein-typed molybdenum deposit in Songxian county, Henan

province. Geoscience 24 (1), 26–33 (in Chinese with English Abstract).
Bajwah, Z., Seccombe, P., Offler, R., 1987. Trace element distribution Co: Ni ratios and genesis of the Big Cadia iron-copper deposit, New South Wales, Australia. Miner. Deposita 22, 292–300.
Bao, Z., Sun, W., Zartman, R.E., Yao, J., Gao, X., 2017. Recycling of subducted upper continental crust: constraints on the extensive molybdenum mineralization in the Qinling-Dabie Orogen. Ore Geol. Rev. 81, 451–465.
Bralia, A., Sabatini, G., Troja, F., 1979. A revaluation of the Co/Ni ratio in pyrite as geochemical tool in ore genesis problems. Miner. Deposita 14, 353–374.
Butler, I.B., Rickard, D., 2000. Framboidal pyrite formation via the oxidation of iron (II) monosulfide by hydrogen sulphide. Geochim. Cosmochim. Acta 64, 2665–2672.
Cao, H.-W., Zhang, S.-T., Santosh, M., Zheng, L., Tang, L., Li, D., Zhang, X.-H., Zhang, Y.-H., 2015. The luanchuan Mo-W-Pb-Zn-Ag magmatic-hydrothermal system in the East Qinling metallogenic belt, China: constrains on metallogenesis from C-H-O-S-Pb isotope compositions and Rb-Sr isochron ages. J. Asian Earth Sci. 111, 751–780.
Cao, J., Ye, H.-S., Li, H.-Y., Li, Z.-Y., Zhang, X.-K., He, W., 2014. Geological characteristics and molybdenite Re-Os isotopic dating of Huangshuian carbonatite vein-type mo (Pb) deposit in Songxian County, Henan Province. Miner. Deposits (in Chinese with English Abstract).
Chen, S.-Z., 2009. Geological characteristics and prospecting criteria of molybdenum deposits in Shapoling in Luoning County. Huabei Land Resour. 2, 1–3 (in Chinese with English Abstract).
Chen, X., Ye, H., Wang, H., 2014a. Genesis and evolution of the Leimengou porphyry Mo deposit in West Henan Province, East Qinling-Dabie belt, China: constraints from hydrothermal alteration, fluid inclusions and stable isotope data. J. Asian Earth Sci. 79, 710–722.
Chen, Y., Li, C., Zhang, J., Li, Z., Wang, H., 2000. Sr and O isotopic characteristics of porphyries in the Qinling molybdenum deposit belt and their implication to genetic mechanism and type. Sci. China Ser. D: Earth Sci. 43, 82 (in Chinese with English Abstract).
Chen, Y.-J., Pirajno, F., Li, N., Guo, D.-S., Lai, Y., 2009b. Isotope systematics and fluid inclusion studies of the Qiyugou breccia pipe-hosted gold deposit, Qinling Orogen, Henan province, China: implications for ore genesis. Ore Geol. Rev. 35, 245–261.
Chen, Y.-J., Pirajno, F., Qi, J.-P., 2008. The Shanggong gold deposit, Eastern Qinling Orogen, China: isotope geochemistry and implications for ore genesis. J. Asian Earth Sci. 33, 252–266.
Chen, Y.-J., Pirajno, F., Sui, Y.-H., 2004. Isotope geochemistry of the Tieluping silver-lead deposit, Henan, China: a case study of orogenic silver-dominated deposits and related tectonic setting. Miner. Deposita 39, 560–575.
Chen, Y.-J., Santosh, M., Somerville, I., Chen, H.-Y., 2014b. Indosinian tectonics and mineral systems in China: an introduction. Geol. J. 49, 331–337.
Ciobanu, C.L., Cook, N.J., Utsunomiya, S., Kogagwa, M., Green, L., Gilbert, S., Wade, B., 2012. Gold-telluride nanoparticles revealed in arsenic-free pyrite. Am. Miner. 97, 1515–1518.
Cook, N.J., Spry, P., Vokes, F., 1998. Mineralogy and textural relationships among sulphosalts and related minerals in the Bleikvassli Zn-Pb-(Cu) deposit, Nordland, Norway. Miner. Deposita 34, 35–56.
Cook, N.J., Ciobanu, C.L., Danyushevsky, L.V., Gilbert, S., 2011. Minor and trace elements in bornite and associated Cu-(Fe)-sulfides: a LA-ICP-MS studyBornite mineral chemistry. Geochim. Cosmochim. Acta 75, 6473–6496.
Cook, N.J., Ciobanu, C.L., Mao, J., 2009a. Textural control on gold distribution in As-free pyrite from the Dongping, Huangtuliang and Hougou gold deposits, North China Craton (Hebei Province, China). Chem. Geol. 264, 101–121.
Cook, N.J., Ciobanu, C.L., Pring, A., Skinner, W., Shimizu, M., Danyushevsky, L., Saini-Eidukat, B., Melcher, F., 2009b. Trace and minor elements in sphalerite: a LA-ICP-MS study. Geochim. Cosmochim. Acta 73, 4761–4791.
Cui, M.-L., Zhang, B.-L., Liang, G.-H., Cai, X.-P., Wang, J., Gao, H.-Z., et al., 2006. Ore-prospecting vista of concealed polymetallic deposits in Shapoling of Luoning, Western Henan. Miner. Deposits S1, 467–470 (in Chinese with English Abstract).
Deditius, A.P., Utsunomiya, S., Reich, M., Kesler, S.E., Ewing, R.C., Hough, R., Walshe, J., 2011. Trace metal nanoparticles in pyrite. Ore Geol. Rev. 42, 32–46.
Deditius, A.P., Utsunomiya, S., Renock, D., Ewing, R.C., Ramana, C.V., Becker, U., Kesler, S.E., 2008. A proposed new type of arsenian pyrite: composition, nanostructure and geological significance. Geochim. Cosmochim. Acta 72, 2919–2933.
Deng, J., Gong, Q., Wang, C., Carranza, E.J.M., Santosh, M., 2014a. Sequence of late Jurassic-Early cretaceous magmatic-hydrothermal events in the Xiong'ershan region, Central China: an overview with new zircon U-Pb geochronology data on quartz porphyries. J. Asian Earth Sci. 79, 161–172.
Deng, X.-H., Chen, Y.-J., Bagas, L., Zhou, H.-Y., Yao, J.-M., Zheng, Z., Wang, P., 2015. Isotope (S-Sr-Nd-Pb) constraints on the genesis of the ca. 850 Ma tumen Mo-F deposit in the Qinling Orogen, China. Precambr. Res. 266, 108–118.
Deng, X.-H., Chen, Y.-J., Pirajno, F., Li, N., Yao, J.-M., Sun, Y.-L., 2017. The geology and geochronology of the Waifangshan Mo-quartz vein cluster in eastern Qinling, China. Ore Geol. Rev. 81, 548–564.
Deng, X.-H., Chen, Y.-J., Santosh, M., Yao, J.-M., Sun, Y.-L., 2016. Re-Os and Sr-Nd-Pb isotope constraints on source of fluids in the Zhifang Mo deposit, Qinling Orogen, China. Gondwana Res. 30, 132–143.
Deng, X.-H., Chen, Y.-J., Yao, J.-M., Bagas, L., Tang, H.-S., 2014b. Fluorite REE-Y (REY) geochemistry of the ca. 850 Ma Tumen molybdenite-fluorite deposit, eastern Qinling, China: constraints on ore genesis. Ore Geol. Rev. 63, 532–543.
Deng, X.-H., Chen, Y., Santosh, M., Yao, J., 2013a. Genesis of the 1.76 Ga Zhaiwa Mo-Cu and its link with the Xiong'er volcanics in the North China Craton: implications for accretionary growth along the margin of the Columbia supercontinent. Precambr. Res. 227, 337–348.
Deng, X.-H., Chen, Y., Santosh, M., Zhao, G., Yao, J., 2013b. Metallogeny during continental outgrowth in the Columbia supercontinent: isotopic characterization of the Zhaiwa Mo-Cu system in the North China Craton. Ore Geol. Rev. 51, 43–56.
Deng, X.-H., Chen, Y.-J., Santosh, M., Yao, J.-M., 2013c. Re-Os geochronology, fluid inclusions and genesis of the 0.85 Ga Tumen molybdenite-fluorite deposit in Eastern Qinling, China: implications for pre-Mesozoic Mo enrichment and tectonic setting. Geol. J. 48, 484–497.
Deng, X.-H., Santosh, M., Yao, J.-M., Chen, Y.-J., 2014c. Geology, fluid inclusions and sulphur isotopes of the Zhifang Mo deposit in Qinling Orogen, central China: a case study of orogenic-type Mo deposits. Geol. J. 49, 515–533.
Dong, Y., Santosh, M., 2016. Tectonic architecture and multiple orogeny of the Qinling Orogenic Belt, Central China. Gondwana Res. 29, 1–40.
Fan, H.-R., Hu, F.-F., Wilde, S.A., Yang, K.-F., Jin, C.-W., 2011. The Qiyugou gold-bearing breccia pipes, Xiong'ershan region, central China: fluid-inclusion and stable-isotope evidence for an origin from magmatic fluids. Int. Geol. Rev. 53, 25–45.
Fan, H.-R., Xie, Y.-H., Zhao, R., Wang, Y.L., 1994. Stable isotope geochemistry of rocks and gold deposits in the Xiongershan area western Henan province. Contrib. Geol. Miner. Resour. Res. 9 (1), 54–64 (in Chinese with English Abstract).
Gao, Y.-F., Luan, W.-L., 1994. Stable isotope studies of gold deposits in Qiyugou area, Henan province. Miner. Deposits 13, 354–362 (in Chinese with English Abstract).
Han, Y.G., Zhang, S.H., Pirajno, P., Zhang, Y.H., 2007a. Evolution of the Mesozoic granites in the Xiong'ershan-Waifangshan region, western Henan province, China, and its tectonic implications. Acta Geol. Sin. Engl. Ed. 81, 253–265.
Han, Y., Li, X., Zhang, S., Zhang, Y., Chen, F., 2007b. Single grain Rb-Sr dating of euhedral and cataclastic pyrite from the Qiyugou gold deposit in western Henan, central China. Chin. Sci. Bull. 52, 1820–1826 (in Chinese with English Abstract).
Han, Y., Zhang, S., Pirajno, F., Wang, Y., Zhang, Y., 2009. New 40Ar-39Ar age constraints on the deformation along the Machaoying fault zone: implications for Early Cambrian tectonism in the North China Craton. Gondwana Res. 16, 255–263.
Huang, D.-H., Du, A.-D., 1994. Re-os isotope ages of molybdenum deposits in east Qinling and their significance. Chin. J. Geochem. 14 (4), 313–322 (in Chinese with English Abstract).
Huang, D.-H., Hou, Z.-Q., Yang, Z.-M., Li, Z.-Q., Xu, D.-X., 2009. Geological and geochemical characteristics, metallogenetic mechanism and tectonic setting of carbonatite vein-type Mo(Pb) deposits in the East Qinling molybdenum ore belt. Acta Geol. Sin. 83 (12), 1968–1984 (in Chinese with English Abstract).
Huerta-Diaz, M.A., Morse, J.W., 1992. Pyritization of trace metals in anoxic marine sediments. Geochim. Cosmochim. Acta 56, 2681–2702.
Koglin, N., Frimmel, H.E., Minter, W.L., Brätz, H., 2010. Trace-element characteristics of different pyrite types in Mesoarchaean to Palaeoproterozoic placer deposits. Miner. Deposita 45, 259–280.
LaFlamme, C., Martin, L., Jeon, H., Reddy, S.M., Selvaraja, V., Caruso, S., Bui, T.H., Roberts, M.P., Voute, F., Hagemann, S., 2016. In situ multiple sulfur isotope analysis by SIMS of pyrite, chalcopyrite, pyrrhotite, and pentlandite to refine magmatic ore genetic models. Chem. Geol. 444, 1–15.
LaFlamme, C., Jamieson, J.W., Fiorentini, M.L., Thebaud, N., Caruso, S., Selvaraja, V., 2018. Investigating sulfur pathways through the lithosphere by tracing mass independent fractionation of sulfur to the Lady Bountiful orogenic gold deposit, Yilgarn Craton. Gondwana Res. 58, 27–38.
Large, R.R., Danyushevsky, L., Hollit, C., Maslennikov, V., Meffre, S., Gilbert, S., Bull, S., Scott, R., Emsbo, P., Thomas, H., 2009. Gold and trace element zonation in pyrite using a laser imaging technique: implications for the timing of gold in orogenic and Carlin-style sediment-hosted deposits. Econ. Geol. 104, 635–668.
Li, D., Han, J.-W., Zhang, S.-T., Yan, C.-H., Cao, H.-W., Song, Y.-W., 2015. Temporal evolution of granitic magmas in the Luanchuan metallogenic belt, east Qinling Orogen, central China: implications for Mo metallogenesis. J. Asian Earth Sci. 111, 663–680.
Li, D., Zhang, S.-T., Yan, C.-H., Wang, G.-W., Song, Y.-W., Ma, Z.-B., Han, J.-W., 2012. Late Mesozoic time constraints on tectonic changes of the Luanchuan Mo belt, East Qinling orogen, Central China. J. Geodyn. 61, 94–104.
Li, N., Chen, Y.J., Zhang, H., Zhao, T., Deng, X.H., Wang, Y., 2007. Molybdenum deposits in east qinling. Earth Sci. Front. 14 (5), 186–198 (in Chinese with English Abstract).
Li, N., Pirajno, F., 2017. Early Mesozoic Mo mineralization in the Qinling Orogen: an overview. Ore Geol. Rev. 81, 431–450.
Li, R., Chen, H., Xia, X., Yang, Q., Li, L., Xu, J., Huang, C., Danyushevsky, L.V., 2017a. Ore fluid evolution in the giant Marcona Fe-(Cu) deposit, Perú: evidence from in-situ sulfur isotope and trace element geochemistry of sulfides. Ore Geol. Rev. 86, 624–638.
Li, S., Zhao, S., Liu, X., Cao, H., Yu, S., Li, X., Somerville, I., Yu, S., Suo, Y., 2017b. Closure of the Proto-Tethys Ocean and Early Paleozoic amalgamation of microcontinental blocks in East Asia. Earth Sci. Rev. https://doi.org/10.1016/j.earscirev.2017.01.011.
Li, Y.-F., Mao, J.-W., Liu, D., Wang, Y., Wang, Z., Wang, Y., 2006. SHRIMP zircon U-Pb and molybdenite Re-Os datings for the Leimengou porphyry molybdenum deposit, western Henan and its geological implication. Geol. Rev. 52 (1), 122–131 (in Chinese with English Abstract).
Li, Y.-F., 2005. The Temporal-spatial Evolution of Mesozoic Granitoids in the Xiong'ershan Area and their Relationships to Molybdenum-gold Mineralization (Doctor Dissertation). China University of Geosciences, Beijing, pp. 1–143.
Li, Z.-K., Li, J.-W., Cooke, D.R., Danyushevsky, L., Zhang, L., O'Brien, H., Lahaye, Y., Zhang, W., Xu, H.-J., 2016. Textures, trace elements, and Pb isotopes of sulfides from the Haopinggou vein deposit, southern North China Craton: implications for discrete Au and Ag-Pb-Zn mineralization. Contrib. Miner. Petrol. 171, 99.
Li, Z.-K., Li, J.-W., Zhao, X.-F., Zhou, M.-F., Selby, D., Bi, S.-J., Sui, J.-X., Zhao, Z.-J., 2013. Crustal-extension Ag-Pb-Zn veins in the Xiong'ershan District, Southern North China craton: constraints from the Shagou deposit. Econ. Geol. 108, 1703–1729.
Liu, J., Wu, G., Jia, S.-M., Li, Z.-Q., Sun, Y.-L., Zhong, W., Zhu, M.-T., 2011. Re-Os isotopic dating of molybdenites from the Shapoling molybdenum deposit in western Henan Province and its geological significance. J. Mineral. Petrol. 31 (1), 56–62 (in Chinese

with English Abstract).
Lu, X.-X., Luo, Z.-H., Huang, F., Liang, T., Huang, D.-F., Han, N., Gao, Y., 2017. "Small" magma and "big" fluid lead to form large scale deposit and transmagmatic fluid mineralization: take for example of Mo deposits in eastern Qinling-Dabie mountain metallogenic belt. Acta Petrol. Sin. 33 (5), 1554–1570 (in Chinese with English Abstract).
Mao, J., Goldfarb, R.J., Zhang, Z., Xu, W., Qiu, Y., Deng, J., 2002. Gold deposits in the Xiaoqinling-Xiong'ershan region, Qinling Mountains, central China. Miner. Deposita 37, 306–325.
Mao, J., Pirajno, F., Xiang, J., Gao, J., Ye, H., Li, Y., Guo, B., 2011. Mesozoic molybdenum deposits in the east Qinling-Dabie orogenic belt: characteristics and tectonic settings. Ore Geol. Rev. 43, 264–293.
Mao, J., Xie, G., Bierlein, F., Qü, W., Du, A., Ye, H., Pirajno, F., Li, H.M., Guo, B., Li, Y., 2008. Tectonic implications from Re-Os dating of Mesozoic molybdenum deposits in the East Qinling-Dabie orogenic belt. Geochim. Cosmochim. Acta 72, 4607–4626.
Mao, J., Xie, G., Pirajno, F., Ye, H., Wang, Y., Li, Y., Xiang, J., Zhao, H., 2010. Late Jurassic-Early Cretaceous granitoid magmatism in Eastern Qinling, central-eastern China: SHRIMP zircon U-Pb ages and tectonic implications. Aust. J. Earth Sci. 57, 51–78.
Mao, J.-W., Zhang, Z.-C., Zhang, Z.-H., Andao, D., 1999. Re-Os isotopic dating of molybdenites in the Xiaoliugou W (Mo) deposit in the northern Qilian mountains and its geological significance. Geochim. Cosmochim. Acta 63, 1815–1818.
Maslennikov, V., Maslennikova, S., Large, R., Danyushevsky, L., 2009. Study of trace element zonation in vent chimneys from the Silurian Yaman-Kasy volcanic-hosted massive sulfide deposit (Southern Urals, Russia) using laser ablation-inductively coupled plasma mass spectrometry (LA-ICPMS). Econ. Geol. 104, 1111–1141.
Morse, J., Luther Iii, G., 1999. Chemical influences on trace metal-sulfide interactions in anoxic sediments. Geochim. Cosmochim. Acta 63, 3373–3378.
Neumayr, P., Walshe, J., Hagemann, S., Petersen, K., Roache, A., Frikken, P., Horn, L., Halley, S., 2008. Oxidized and reduced mineral assemblages in greenstone belt rocks of the St. Ives gold camp, Western Australia: vectors to high-grade ore bodies in Archaean gold deposits? Miner. Deposita 43, 363–371.
Ohmoto, H., 1979. In: Isotopes of Sulfur and Carbon. Geochemistry of Hydrothermal ore Deposits, pp. 509–567.
Ohmoto, H., 1986. Stable isotope geochemistry of ore deposits. Rev. Miner. 16, 491–560.
Palme, H., O'Neill, H.S.C., 2003. Cosmochemical estimates of mantle composition. Treatise Geochem. 2, 568.
Price, B.J., 1972. Minor Elements in Pyrites from the Smithers Map area, Bc and Exploration Applications of Minor Element Studies. University of British Columbia.
Reich, M., Chryssoulis, S.L., Deditius, A., Palacios, C., Zuniga, A., Weldt, M., Alvear, M., 2010. "Invisible" silver and gold in supergene digenite (Cu1. 8S). Geochim. Cosmochim. Acta 74, 6157–6173.
Reich, M., Deditius, A., Chryssoulis, S., Li, J.-W., Ma, C.-Q., Parada, M.A., Barra, F., Mittermayr, F., 2013. Pyrite as a record of hydrothermal fluid evolution in a porphyry copper system: a SIMS/EMPA trace element study. Geochim. Cosmochim. Acta 104, 42–62.
Ren, F.-G., Yin, Y.-J., Li, S.-B., Zhao, J.-N., 2001. The coupling character between isotopic geochronology of Indosinian Epoch in Xiong'er fault basin. Bull. Mineral. Petrol. Geochem. 20, 286–288 (in Chinese with English Abstract).
Rudnick, R., Gao, S., 2003. Composition of the continental crust. Treatise Geochem. 3, 659.
Stein, H., Markey, R., Morgan, J., Du, A., Sun, Y., 1997. Highly precise and accurate Re-Os ages for molybdenite from the East Qinling molybdenum belt, Shaanxi Province, China. Econ. Geol. 92, 827–835.
Stein, H., Markey, R., Morgan, J., Hannah, J., Scherstén, A., 2001. The remarkable Re-Os chronometer in molybdenite: how and why it works. Terra Nova 13, 479–486.
Su, J., Zhang, B.-L., Sun, D.-H., Cui, M.-L., Qu, W.-J., Du, A.-D., 2009. Geological features and Re-Os isotopic dating of newly discovered Shapoling veinlet-disseminated Mo deposit in the eastern section of East Qinling Mountains and its geological significance. Acta Geol. Sin. 83, 1490–1496 (in Chinese with English Abstract).
Tang, L., Santosh, M., Dong, Y., 2015. Tectonic evolution of a complex orogenic system: evidence from the northern Qinling belt, central China. J. Asian Earth Sci. 113, 544–559.
Tang, L., Santosh, M., Dong, Y., Tsunogae, T., Zhang, S., Cao, H., 2016. Early Paleozoic tectonic evolution of the North Qinling orogenic belt: evidence from geochemistry, phase equilibrium modeling and geochronology of metamorphosed mafic rocks from the Songshugou ophiolite. Gondwana Res. 30, 48–64.
Tang, L., Zhang, S.T., Yang, F., Santosh, M., Li, J.J., Kim, S., Hu, X.K., Zhao, Y., Cao, H.W., 2018. Triassic alkaline magmatism and mineralization in the Xiong'ershan area, East Qinling, China. Geol. J. https://doi.org/10.1002/gj.3166.
Tanner, D., Henley, R.W., Mavrogenes, J.A., Holden, P., 2016. Sulfur isotope and trace element systematics of zoned pyrite crystals from the El Indio Au-Cu-Ag deposit, Chile. Contrib. Miner. Petrol. 171, 33.
Thomas, H.V., Large, R.R., Bull, S.W., Maslennikov, V., Berry, R.F., Fraser, R., Froud, S., Moye, R., 2011. Pyrite and pyrrhotite textures and composition in sediments, laminated quartz veins, and reefs at Bendigo gold mine, Australia: insights for ore genesis. Econ. Geol. 106, 1–31.
Tian, Y., Sun, J., Ye, H., Mao, J., Wang, X., Bi, M., Xia, X., 2017. Genesis of the Dianfang breccia-hosted gold deposit, western Henan Province, China: constraints from geology, geochronology and geochemistry. Ore Geol. Rev. 91, 963–980.
Tribovillard, N., Algeo, T.J., Lyons, T., Riboulleau, A., 2006. Trace metals as paleoredox and paleoproductivity proxies: an update. Chem. Geol. 232, 12–32.
Ulrich, T., Long, D., Kamber, B., Whitehouse, M., 2011. In situ trace element and sulfur isotope analysis of pyrite in a paleoproterozoic gold placer deposit, Pardo and Clement Townships, Ontario, Canada. Econ. Geol. 106, 667–686.
Wang, C., Bagas, L., Chen, J., Yang, L., Zhang, D., Du, B., Shi, K., 2018. The genesis of the Liancheng Cu–Mo deposit in the Lanping Basin of SW China: constraints from geology, fluid inclusions, and Cu–S–H–O isotopes. Ore Geol. Rev. 92, 113–128.
Wang, C., Chen, L., Bagas, L., Lu, Y., He, X., Lai, X., 2016c. Characterization and origin of the Taishanmiao aluminous A-type granites: implications for Early Cretaceous lithospheric thinning at the southern margin of the North China Craton. Int. J. Earth Sci. 105 (5), 1563–1589.
Wang, C., Deng, J., Bagas, L., Wang, Q., 2017a. Zircon Hf-isotopic mapping for understanding crustal architecture and metallogenesis in the Eastern Qinling Orogen. Gondwana Res. 50, 293–310.
Wang, C., Deng, J., Carranza, E.J.M., Santosh, M., 2014b. Tin metallogenesis associated with granitoids in the southwestern Sanjiang Tethyan Domain: nature, deposit types, and tectonic setting. Gondwana Res. 26 (2), 576–593.
Wang, C., Lu, Y., He, X., Wang, Q., Zhang, J., 2016b. The Paleoproterozoic diorite dykes in the southern margin of the North China Craton: insight into rift-related magmatism. Precambr. Res. 277, 26–46.
Wang, C., Song, S., Niu, Y., Wei, C., Su, L., 2016a. TTG and potassic granitoids in the Eastern North China craton: making Neoarchean upper continental crust during micro-continental collision and post-collisional extension. J. Petrol. 57, 1775–1810.
Wang, C., Yang, L., Bagas, L., Evans, N.J., Chen, J., Du, B., 2017c. Mineralization processes at the giant Jinding Zn-Pb deposit, Lanping Basin, Sanjiang Tethys Orogen: evidence from in situ trace element analysis of pyrite and marcasite. Geol. J. https://doi.org/10.1002/gj.2956.
Wang, C., Zhang, D., Wu, G., Santosh, M., Zhang, J., Xu, Y., Zhang, Y., 2014a. Geological and isotopic evidence for magmatic-hydrothermal origin of the Ag–Pb–Zn deposits in the Lengshuikeng District, east-central China. Miner. Deposita 49 (6), 733–749.
Wang, R., Cudahy, T., Laukamp, C., Walshe, J.L., Bath, A., Mei, Y., Young, C., Roache, T.J., Jenkins, A., Roberts, M., 2017b. White mica as a hyperspectral tool in exploration for the sunrise dam and Kanowna Belle gold deposits, Western Australia. Econ. Geol. 112, 1153–1176.
Wang, Y., Mao, J., Lu, X., 2001. ^{40}Ar-^{39}Ar dating and geochronological constraints on the ore-forming epoch of the Qiyugou gold deposit in Songxian County, Henan Province. Geol. Rev. 47, 551–555.
Ward, J., Mavrogenes, J., Murray, A., Holden, P., 2017. Trace element and sulfur isotopic evidence for redox changes during formation of the Wallaby Gold Deposit, Western Australia. Ore Geol. Rev. 82, 31–48.
Wen, S.-P., Liu, G.-Y., Qiao, B.-L., Liu, S.-F., Zheng, F.-X., 2008. Geological characteristics and ore-prospecting direction of zhifang molybdenum deposit in songxian. China Molybdenum Ind. 32, 14–17 (in Chinese with English Abstract).
Xiao, E., Jian, H., Zhang, Z.-Z., Dai, B.-Z., Wang, Y.-F., Li, H.-Y., 2012. Petrogeochemistry, zircon U-Pb dating and Lu-Hf isotopic compositions of the Haoping and Jinshanmiao granites from the Huashan complex batholith in eastern Qinling Orogen. Acta Petro. Sin. 28 (12), 4031–4046 (in Chinese with English Abstract).
Xue, Y., Campbell, I., Ireland, T.R., Holden, P., Armstrong, R., 2013. No mass-independent sulfur isotope fractionation in auriferous fluids supports a magmatic origin for Archean gold deposits. Geology 41, 791–794.
Yan, J., Hu, R., Liu, S., Lin, Y., Zhang, J., Fu, S., 2018. NanoSIMS element mapping and sulfur isotope analysis of Au-bearing pyrite from Lannigou Carlin-type Au deposit in SW China: new insights into the origin and evolution of Au-bearing fluids. Ore Geol. Rev. 92, 29–41.
Yao, J.-M., Zhao, T.-P., Li, J., Sun, Y.-L., Yun, Z.-L., Chen, W., Han, J., 2009. Molybdenite Re-Os age and zircon U-Pb age and Hf isotope geochemistry of the Qiyugou gold system, Henan Province. Acta Petro. Sin. 25 (2), 374–384.
Zhang, J., Deng, J., Chen, H.-Y., Yang, L.-Q., Cooke, D., Danyushevsky, L., Gong, Q.-J., 2014. LA-ICP-MS trace element analysis of pyrite from the Chang'an gold deposit, Sanjiang region, China: implication for ore-forming process. Gondwana Res. 26, 557–575.
Zhang, Y., Cao, H., Xu, M., Zhang, S., Tang, L., Wang, S., Pei, Q., Cai, G., Shen, T., 2017. Petrogenesis of the late Mesozoic highly fractionated I-type granites in the Luanchuan district: implications for the tectono-magmatic evolution of eastern Qinling. Geosci. J. 1–20.
Zhang, Y., Zhang, S., Xu, M., Jiang, X., Li, J., Wang, S., Li, D., Cao, H., Zou, H., Fang, Y., 2015. Geochronology, geochemistry, and Hf isotopes of the Jiudinggou molybdenum deposit, Central China, and their geological significance. Geochem. J. 49, 321–342.
Zhang, Z., Yang, X., Dong, Y., Zhu, B., Chen, D., 2011. Molybdenum deposits in the eastern Qinling, central China: constraints on the geodynamics. Int. Geol. Rev. 53, 261–290.
Zhao, H.-X., Dai, B.-Z., Li, B., Zhu, Z.-Y., 2015. Genesis of the checangyu molybdenum deposit in the xiaoqinling district: constraints from the re-os dating of molybdenite and in situ trace element analysis of pyrite. Acta Petrol. Sin. 31 (3), 784–790 (in Chinese with English Abstract).
Zhao, H.-X., Frimmel, H.E., Jiang, S.-Y., Dai, B.-Z., 2011. LA-ICP-MS trace element analysis of pyrite from the Xiaoqinling gold district, China: implications for ore genesis. Ore Geol. Rev. 43, 142–153.